Journal of Sound and Vibration 581 (2024) 118378

Contents lists available at ScienceDirect

Journal of Sound and Vibration

journal homepage: www.elsevier.com/locate/jsvi

A direct multimode method for the reduction of vibration induced oscillations on force signals during "pseudo-rigid" water impact experiments

Alan Tassin [a,*], Florian Hulin [a,b,c], Nicolas Jacques [b]

[a] Ifremer, RDT, F-29280, Plouzané, France
[b] ENSTA Bretagne, UMR CNRS 6027, IRDL, 29806, Brest CEDEX 09, France
[c] France Énergies Marines, Technopôle Brest-Iroise, 525 Avenue Alexis de Rochon, 29280, Plouzané, France

ARTICLE INFO

Keywords:
Vibrations
Hydroelasticity
Water impact
Fluid–structure interaction

ABSTRACT

A new experimental method is proposed to improve the force measurements during water impact experiments (*e.g.* water entry or wave impact tests) carried out with "pseudo-rigid" mock-ups. Despite the efforts of making the mock-up as stiff as possible, the impulsive nature of water impact loads may induce a transient response of the mock-up with a broad frequency content and a perturbation of the force measurements. Using the principles of momentum conservation, it can be shown that the load cell signal is the sum of the hydrodynamic forcing term and of an additional inertial term directly related to the vibrations of the structure. In the present paper, we suggest to estimate the inertial term using several accelerometers which record the response of the structure at different locations. Assuming that the structure response can be approximated by a set of natural modes, we show that it is possible to estimate the inertial term by a linear combination of the acceleration signals. The coefficients of the linear combination may be identified *a priori* by performing hammer tests, but in certain cases they can also be identified *a posteriori* using a segment of the signal time series. The performance of the method is demonstrated by considering two experimental test cases of increasing complexity. The first test case is a hydrofoil of constant section impacting water at constant speed which exhibits two-dimensional beam-like vibrations. The second test case is a segmented model of a vertical cylinder impacted by a breaking wave whose segments exhibit three-dimensional vibrations. The proposed method is efficient, conceptually simple and very simple to implement from a signal processing point of view, which makes it promising not only for water impact problems but also for other unstationary fluid–structure interaction problems.

1. Introduction

Water impact loads are well known for being very large in magnitude and very short in time. Due to their impulsive nature, they can induce high-frequency vibrations of marine structures. Water impacts on ships induce the so-called whipping phenomenon which is of major concern for the ship industry [see 1,2]. Offshore wind turbines and lighthouses are also subject to high-frequency vibrations induced by breaking wave impact loads [see 3,4]. Interestingly, the vibrations are also exploited to detect water impact events and to estimate the impact loads on full-scale structures via acceleration recordings [see 3–5].

* Corresponding author.
E-mail address: alan.tassin@ifremer.fr (A. Tassin).

https://doi.org/10.1016/j.jsv.2024.118378
Received 20 July 2023; Received in revised form 1 March 2024; Accepted 3 March 2024
Available online 4 March 2024

Despite the progress of high-fidelity numerical simulation methods, the numerical simulation of this type of complex hydroelastic problems remains delicate and requires careful validation against analytical and/or experimental results. In order to assess the ability of a theoretical (numerical or analytical) model to accurately simulate the fluid flow and to predict accurately the water impact loads, it is common practice to run "simple" validation test cases where the body entering water is assumed to be rigid, the water surface is initially at rest and the body is moving with a constant speed. Although it is crucial to perform experiments in order to validate these models, a perfectly rigid impactor does not exist in reality and many experimental investigations aiming at measuring the hydrodynamic force during water impact experiments are affected by the vibrations of the impactor and/or the test-rig. Campbell and Weynberg [6] already highlighted the difficulty of measuring the force acting on a circular cylinder impacting water. In fact, despite their efforts to increase the stiffness of their set-up, the maximum force recorded by the load cell is amplified by a factor of almost 2 due to the dynamic response of the structure. These difficulties are particularly acute in two-dimensional experiments with blunt bodies (*e.g.* circular cylinder) due to the discontinuous nature of the water impact force. Indeed, the two-dimensional incompressible theory of Wagner predicts that the force jumps from a value of 0 to its maximum value at the first instant of the impact for a two-dimensional blunt body. Measuring the impact force on a circular cylinder remains challenging, as illustrated in Moalemi et al. [7] where the force measurements are clearly affected by the vibrations of the test-rig. Experiments with wedges and cones are less prone to vibration because the force evolution is smoother. Double-curvature body-shapes (*e.g.* elliptic paraboloïd, sphere) are less prone to vibrations than single-curvatures body-shapes (*e.g.* circular cylinder), but some vibration-induced oscillations on the force signals have been observed in the experiments of Tassin et al. [8] with an elliptic paraboloïdal shape. The vibrations observed in the experiments may also result from the actuators or motion generator used to put the model in motion [see 9,10]. At very high speeds as in the large scale high-speed ditching facility of CNR-INM [11], the magnitudes of the forces and accelerations are so high that vibrations are likely to appear. Indeed, Iafrati et al. [12] mention the oscillations of the guiding structure as a possible source of data scatter. Some of the force recordings published in Iafrati and Grizzi [11] present a rather high level of oscillations which, although not mentioned by the authors, may also be a result of the vibrations of the guide or the model. In the water exit experiments of Vega-Martínez et al. [13], it was shown necessary to take into account the hydro-elastic interactions in order to match the experimental force results with the theoretical ones despite the use of a rather stiff model. Sloshing experiments are extensively used to design the tanks of the Liquid Natural Gas (LNG) transport ships which are subject to violent water impacts. These tests are typically conducted using a six degree-of-freedom motion generator in order to emulate the motion of the ship. In these experiments, in addition to local pressure measurements, it is also interesting to measure the global force exerted by the liquid tank on the motion generator in order to validate liquid motion simulations and to study the interaction between the tank and the ship motion. For example, Diebold and Baudin [14] published global force measurements for a single wave impact. In these experiments, the motion generator starts moving with a very simple motion and a single wave impact occurs just before the motion generator stops moving. In the recordings (see Figs. 14 and 15), one can clearly see that the force measurements exhibit moderate high-frequency oscillations before the impact, these oscillations increase suddenly when the impact occurs and then they almost vanish as soon as the motion generator stops. This example clearly highlights the effect of the vibrations of the set-up which is excited by the motion generator and the water impact event.

Wave tank experiments are also conducted to validate the theoretical models used to predict breaking-wave impact loads on offshore and coastal structures. This complex phenomenon is very difficult to simulate numerically and therefore it is important to compare the numerical results against reliable experimental results. Despite the rather well controlled conditions in laboratory experiments, the measurement of breaking-wave impact loads in laboratory experiments is very challenging. In addition to the high sensitivity of the breaking-wave impact phenomenon to small perturbations in the experimental conditions [see 15], the dynamic response of the structure reported in different experimental investigations makes it difficult to measure accurately the hydrodynamic forcing loads. In the large-scale experiments of Wienke and Oumeraci [16] dedicated to the measurement of breaking wave impacts on vertical and inclined cylinders, the force measurements are strongly affected by the vibrations of the structure. Vibrations are also highlighted in the experiments of Wang et al. [17] who studied the impact of breaking waves on a jacket structure. Within the WIFI JIP [see18, for an overview], wave tank experiments were conducted with an elastic model representative of a wind turbine monopile in order to record the response of the structure to the breaking wave loads and with a stiff model in order to measure the breaking wave forcing loads. Despite the efforts for building a stiff model for these experiments, Suja-Thauvin et al. [19] wrote: "*During the tests, it was observed that the stiff model was nonetheless responding at times in its 1st mode. The loads measured on the stiff model can therefore not be taken as the excitation loads because they contain the dynamic amplification of the 1st mode of the structure. In order to remove the response of the stiff model from the measured response and keep only the excitation loads, a low-pass 6th order Butterworth filter was applied with a cut-off frequency at 1.2 Hz. This simple technique brings a major limitation: loads from breaking waves typically have very short durations, so by removing high frequencies from the excitation loads, the load contribution from breaking waves is potentially removed as well. The data from the stiff model therefore cannot be used to study slamming loads, but it can be used to examine 2nd and 3rd order loads.*"

This last comment illustrates very well the difficulty of measuring water impact forcing loads, even in controlled laboratory conditions. Dynamic amplification is a well known phenomenon in structure dynamics [see 20] which depends on the ratio between the characteristic time of the forcing load and the natural period of the structure. The dynamic amplification factor tends to a value of 2 in the case of an infinitely long Heaviside-type force evolution whereas it can be lower than 1 if the period of the first natural mode of the mechanical system is much longer than the duration of the impulse. The dynamic amplification phenomenon has been investigated theoretically by Korobkin et al. [21] in the case of an elastic wedge impacting a calm free-surface. It has also clearly been put in evidence in the experiments of Campbell and Weynberg [6] and Wienke and Oumeraci [16]. For impact experiments, it is generally recommended to ensure that the first natural frequency of the mechanical system is much higher than

the frequency content of the excitation force signal to be recorded, so the system has time to respond to the load. This generally leads to vibrations of the system and to very oscillatory force signals. Even when the first natural frequency of the model is rather high, classical low-pass filters (*e.g.* Butterworth, Fourier filters) are not adapted to impulse-type signals as the high-frequency components of the excitation force may be removed. In order to overcome this problem, different authors have used alternative signal processing approaches such as the Empirical Mode Decomposition (EMD) or more physical approaches aiming at inferring the excitation force from the response of the structure (inverse methods). The EMD was used by Spinosa and Iafrati [10] in order to remove vibrations generated by the actuators during ditching experiments and by Choi et al. [22] to remove the dynamic amplification in breaking wave impact experiments. Inverse or deconvolution methods have been used by different authors for different purposes. These methods are meant to be more physical than pure signal processing approaches because they use the mechanical transfer function in order to infer the excitation force from the response of the structure. Wienke and Oumeraci [16] used a basic deconvolution approach where the time evolution of the excitation force is assumed to be known from a slamming model and the magnitude of the excitation force is adjusted such that the simulated maximum force induced by the response of the structure matches the recorded one. Maes et al. [23] and Antonini et al. [4] used more elaborated inverse methods to infer the excitation force from acceleration recordings on monopile-type structures. One may use similar techniques using both force and acceleration signals in order to recover the hydrodynamic excitation force. However, in these approaches, it seems necessary to make some assumptions on the loading. In Maes et al. [23], a particular spatial distribution of the excitation force is assumed while in Antonini et al. [4] both a particular spatial distribution and time evolution of the excitation force are assumed *a priori*. Despite the general formulations presented in Maes et al. [23] and Antonini et al. [4] which can theoretically deal with complex mechanical systems with several degrees of freedom, only the first natural mode is considered in both investigations. From a practical point of view, these techniques may be difficult to use by users unfamiliar with the rather complex concepts behind the techniques.

In the present paper, we propose an alternative approach which consists in subtracting the inertial term of the force resulting from the acceleration field in the elastic body subject to the vibrations. This method is an extension of the method employed by El Malki Alaoui et al. [24] and Breton et al. [9] to compensate for the part of the force due to the acceleration of the model mass (under the rigid body assumption). In El Malki Alaoui et al. [24], the apparent mass of the model (including a part of the sensor) is identified by a calibration procedure before the water entry experiments, and the inertial term of the force is retrieved via the measurement of the model acceleration. In the water entry and exit experiments of Breton et al. [9], the velocity varies significantly and, the motion being very reproducible, the inertial term of the force is directly measured by generating the motion of the experiments in air (without touching the water). This simple idea is generalized here to a deformable body by applying the principles of momentum conservation. By making the well accepted assumption that the deformation of the body can be approximated accurately by a combination of several natural modes of vibration, we show that the inertial term of the force can be approximated by a linear combination of several acceleration signals recording the acceleration of the body in different locations of the body. The number and the arrangement of the accelerometers depend on the modes that should be compensated for. The coefficients of the linear combination represent the product of the modal masses and of the coefficients of the inverse transform that relates the second time-derivative of the modal coordinates and the acceleration signals recorded at different locations of the body. These coefficients can be identified by performing hammer tests before or after the experiments. Alternatively, in some cases, it is possible to use a portion of a test recording to identify these coefficients. Two different test cases are investigated to assess the efficiency of the approach. The first one is a hydrofoil which impacts a calm water surface at constant speed. In that first case, the structure is rather simple and the coefficients have been identified after the experiments using a portion of the signals corresponding to a constant speed stage prior to the impact. The second test case corresponds to a breaking wave impacting a segmented cylinder. The structure of this model is more complex. The mode shapes are clearly three-dimensional and the coefficients are identified by performing hammer tests with an instrumented hammer. Comparisons between the force impulse signal recorded by the hammer and the force reconstructed by the proposed method demonstrate that it is possible to accurately recover the excitation force. In addition to reducing the high-frequency oscillations, the proposed method makes it possible to accurately recover the time evolution of the excitation force. In particular, the time delay due to the response of the structure and the dynamic amplification are compensated for. Given that the method consists in performing a linear combination of different signals, the method is very easy to implement and it is computationally efficient. This makes it a valuable approach for real-time applications which use force measurements to control a system. In contrast to the classical real-time low-pass filters which are used to remove high-frequency oscillations, the proposed method introduces no delay in the signals, which is also of great interest from a control point of view. The results obtained for the two test cases show that the method is promising. It is important to point out that the method has been implemented on these two test cases *a posteriori*, *i.e.* without changing the original design of the set-up. In future, better results could be obtained by orienting the design of the set-up towards a better implementation of the method. In that sense, the proposed method could make experimentalists rethink the way they design experimental set-ups, not only for water impact problems, but also for unstationary fluid–structure interaction problems or structural dynamic problems which are also prone to undesired vibration issues [see for example 25–27].

The article is organized as follows: the proposed methodology is described in Section 2, the methodology is applied to the water impact of a hydrofoil in Section 3 and the case of vertical segmented cylinder impacted by breaking waves is considered in Section 4. Conclusions are drawn in Section 5.

2. Description of the methodology

In this section, we describe the methodology developed to reduce the effect of the impactor vibrations on the force measurements. The theoretical framework is first detailed in Section 2.1. The identification procedure necessary to implement the methodology is described in Section 2.2. The content of the hydrodynamic force in the context of water impact problems is discussed in Section 2.3.

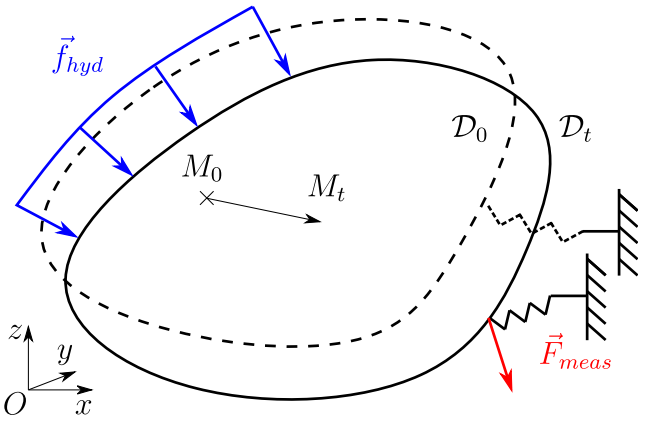

Fig. 1. Deformation of the material domain under an external distributed hydrodynamic force field, $\vec{f}_{hyd}$, of resultant $\vec{F}_{hyd}$ and force measured by the load cell represented as a linear spring, $\vec{F}_{meas}$. The spring (or load cell) may be connected to a fixed or moving body. This boundary condition is represented as a moving clamp.

2.1. Theoretical framework

Let us consider a deformable three-dimensional body subject to an external distributed hydrodynamic force field, $\vec{f}_{hyd}$, of resultant $\vec{F}_{hyd}$ and to a linear restoring force representing the reaction of a typical multi-component load cell, as illustrated in Fig. 1. Vector $\vec{F}_{meas}$ represents the force recorded by the load cell. Initially, the body occupies the material domain $\mathcal{D}_0$ and its configuration at time t is denoted $\mathcal{D}_t$. Function $\vec{T}(x_0, y_0, z_0, t)$ represents the displacement of a material point M_0 in the initial configuration $\mathcal{D}_0$ whose position is defined by vector $O\vec{M}_0 = (x_0, y_0, z_0)$, the frame of reference $(O, \vec{e}_x, \vec{e}_y, \vec{e}_z)$ being fixed in space. Note that the load cell may be connected to a moving body, as it happens when a body enters calm water, or as it may happen on a segmented model where the force is measured on a body (substructure) which is connected to an other structure which may also deform under the loads.

Applying the principles of momentum conservation to the body leads to:

$$\vec{F}_{hyd} - \vec{F}_{meas} = \frac{\mathrm{d}}{\mathrm{d}t}\left(\iiint_{\mathcal{D}_t} \rho(x, y, z, t)\vec{V}(x, y, z, t)\mathrm{d}x\mathrm{d}y\mathrm{d}z\right), \tag{1}$$

where ρ is the current volumic mass of the body and $\vec{V}$ represents the velocity field in the material domain. Making the change of variables $(x, y, z)=(x_0, y_0, z_0) + \vec{T}(x_0, y_0, z_0, t)$ and using the condition of mass conservation ($\rho\mathrm{d}x\mathrm{d}y\mathrm{d}z = \rho_0\mathrm{d}x_0\mathrm{d}y_0\mathrm{d}z_0$), Eq. (1) can be re-written as:

$$\vec{F}_{hyd} - \vec{F}_{meas} = \frac{\mathrm{d}}{\mathrm{d}t}\left(\iiint_{\mathcal{D}_0} \rho_0(x_0, y_0, z_0)\frac{\partial}{\partial t}\vec{T}(x_0, y_0, z_0, t)\mathrm{d}x_0\mathrm{d}y_0\mathrm{d}z_0\right), \tag{2}$$

where ρ_0 is the initial volumic mass of the body. By interchanging the order of integration and differentiation, one finally gets:

$$\vec{F}_{hyd} - \vec{F}_{meas} = \iiint_{\mathcal{D}_0} \rho_0(x_0, y_0, z_0)\frac{\partial^2}{\partial t^2}\vec{T}(x_0, y_0, z_0, t)\mathrm{d}x_0\mathrm{d}y_0\mathrm{d}z_0. \tag{3}$$

Let us now assume that the displacement field can be approximated by a linear combination of N modes of vibration of the body:

$$\vec{T}(x_0, y_0, z_0, t) \approx \sum_{i=1}^{N} a_i(t)\vec{w}_i(x_0, y_0, z_0), \tag{4}$$

where functions $a_i(t)$ represent the time evolution of the modal coordinates and functions $\vec{w}_i(x_0, y_0, z_0)$ represent the mode shapes. Both rigid and elastic modes may be considered. Substituting Eq. (4) into Eq. (3), we obtain:

$$\vec{F}_{hyd} - \vec{F}_{meas} \approx \sum_{i=1}^{N} \ddot{a}_i(t) \underbrace{\iiint_{\mathcal{D}_0} \rho_0(x_0, y_0, z_0)\vec{w}_i(x_0, y_0, z_0)\mathrm{d}x_0\mathrm{d}y_0\mathrm{d}z_0}_{\vec{m}_i}, \tag{5}$$

where the double dot stands for the second time-derivative and vectors $\vec{m}_i$ represent the modal masses of the modes. Therefore, if one were able to measure the modal accelerations, $\ddot{a}_i(t)$, and the modal masses of a sufficiently high number of modes, the hydrodynamic force may be accurately recovered using the following formula:

$$\vec{F}_{hyd}(t) \approx \vec{F}_{meas}(t) + \sum_{i=1}^{N} \ddot{a}_i(t)\vec{m}_i. \tag{6}$$

In order to estimate the second term in the RHS of Eq. (6), we suggest to record the "local" acceleration of the body at N different locations. Following the previous assumption that the displacement field of the body is a linear combination of the first natural modes and under the small perturbation assumption of linear elasticity, the acceleration signals $\gamma_i(t)$ recorded by the accelerometers located at positions $\vec{X}_i$ along the directions $\vec{n}_i$ are linear combinations of the modal acceleration functions, which reads:

$$\gamma_i(t) = \sum_{j=1}^{N} \vec{w}_j(\vec{X}_i) \cdot \vec{n}_i \; \ddot{a}_j(t), \tag{7}$$

or using matrix notations:

$$\underbrace{\begin{bmatrix} \gamma_1(t) \\ \vdots \\ \gamma_N(t) \end{bmatrix}}_{\vec{\Gamma}(t)} = \underbrace{\begin{bmatrix} \vec{w}_1(\vec{X}_1)\cdot\vec{n}_1 & \cdots & \vec{w}_N(\vec{X}_1)\cdot\vec{n}_1 \\ \vdots & \vdots & \vdots \\ \vec{w}_1(\vec{X}_N)\cdot\vec{n}_N & \cdots & \vec{w}_N(\vec{X}_N)\cdot\vec{n}_N \end{bmatrix}}_{\mathbf{W}} \begin{bmatrix} \ddot{a}_1(t) \\ \vdots \\ \ddot{a}_N(t) \end{bmatrix}. \tag{8}$$

Provided that $\mathbf{W}$ is invertible, the hydrodynamic force may be expressed as follows:

$$\vec{F}_{hyd}(t) \approx \vec{F}_{meas}(t) + \mathbf{M}\mathbf{W}^{-1}\vec{\Gamma}(t), \tag{9}$$

where $\mathbf{M}$ is the modal mass matrix defined as:

$$\mathbf{M} = \begin{bmatrix} \vec{m}_1\cdot\vec{e}_x & \cdots & \vec{m}_N\cdot\vec{e}_x \\ \vec{m}_1\cdot\vec{e}_y & \cdots & \vec{m}_N\cdot\vec{e}_y \\ \vec{m}_1\cdot\vec{e}_z & \cdots & \vec{m}_N\cdot\vec{e}_z \end{bmatrix}. \tag{10}$$

The invertibility condition of $\mathbf{W}$ means that the location and orientation of the accelerometers should be chosen according to the shape of the modes which have to be compensated for. Eq. (9) shows that each component of the hydrodynamic force is the sum of the force measured by the load cell and a linear combination of the acceleration signals recorded by the accelerometers. For the x-component of the force F^x, one may write:

$$F^x_{hyd}(t) \approx F^x_{meas}(t) + \sum_{i=1}^{N} \alpha_i^x \gamma_i(t), \tag{11}$$

where the coefficients $(\alpha_1^x, \ldots, \alpha_N^x)$ correspond to the first line of matrix $(\mathbf{M}\mathbf{W}^{-1})$. Similar equations may be obtained for the y- and z-components. For a rigid body, Eq. (9) reduces to:

$$\vec{F}_{hyd}(t) \approx \vec{F}_{meas}(t) + m\vec{\gamma}(t), \tag{12}$$

where m is the mass of the rigid body and $\vec{\gamma}(t)$ is the acceleration of the center of mass of the body. The estimate of the hydrodynamic force obtained from Eq. (11) or (12) will be referred to as the "reconstructed force" in the rest of the paper. In Section 2.2 below, we present a method to identify experimentally the α_i^x coefficients. For a rigid body, it is also important to identify experimentally the mass because a portion of the sensor also contributes to the apparent mass of the system. Equivalent formulas may be derived for the moment induced by the hydrodynamic load by making use of the principles of angular momentum conservation.

2.2. Identification of the reconstruction coefficients

From Eq. (9), one can see that the α_i^x coefficients are independent from the α_i^y and α_i^z coefficients. As such, the identification of the coefficients may be performed independently in each direction. In certain conditions, it may also be worth using a different set of accelerometers for each component. Indeed, some modes may affect only one or two components of the force. As a result, using an accelerometer which is sensitive to an energetic mode to which a particular force component is not sensitive may result in adding "noise" to this particular force component. In the following, we will consider each component individually and the considered force component and reconstruction coefficients will be simply noted F_{hyd} and α_i, respectively. In order to perform the identification, let us consider that we have a synchronized recording of the force and of the different acceleration signals during which the different modes of the structure are excited while the external force, F_{hyd}, is known. Such signals may be obtained by performing a hammer test on the elastic body and selecting a portion of the signal after the impact during which no external force is exerted on the body (F_{hyd}=0). Alternatively, if the body is in motion during the test, a portion of the signal prior to the impact during which the body is vibrating (due to the excitation of the motion generator) may be selected. These two cases will be considered in the application Sections 3 and 4. Let $[t_1, t_2]$ be the time interval during which the external force F_{hyd} is equal to zero. The different signals should satisfy the following condition:

$$F_{meas}(t) + \sum_{i=1}^{N} \alpha_i \gamma_i(t) = 0, \quad t \in [t_1, t_2]. \tag{13}$$

A set of coefficients may be found using a least-square optimization technique such as to minimize the error on Eq. (13), *i.e.* minimizing the cost function ϵ:

$$\epsilon = \sum_{k=1}^{n} \left(F_{meas}(t^k) + \sum_{i=1}^{N} \alpha_i \gamma_i(t^k) \right)^2, \tag{14}$$

where $t^{k=1\to n}$ represent the time-instants at which the signals are discretized such that $t_1 \leq t^k \leq t_2$. Note that it may be necessary to center or detrend the signals in order to retain the frequency content of interest for the identification. This may happen when the sensor signals are drifting or when there is a low frequency hydrodynamic force in the time interval selected for the identification (see Section 3 below). This procedure has been applied to two case studies which are presented in Sections 3 and 4 below. Alternatively, if the identification is performed using an instrumented hammer which records the impact force, the time-interval corresponding to the force impulse may also be used for the identification. In that case, F_{hyd} should be substituted by the force measured by the hammer, F_{ham}, and the cost function becomes:

$$\epsilon = \sum_{k=1}^{n} \left(F_{meas}(t^k) - F_{ham}(t^k) + \sum_{i=1}^{N} \alpha_i \gamma_i(t^k) \right)^2 . \tag{15}$$

2.3. Discussion on the hydrodynamic force in the context of water impacts

In order to validate water impact models and numerical simulations, it is usual to perform experiments with a rigid body which enters an initially calm water tank at constant speed or with a fixed rigid body which is impacted by a wave. In the case of a perfectly rigid body entering water with a varying vertical velocity, $U(t)$, the Wagner theory of water impact [see 28] predicts that the hydrodynamic force, F_{hyd}, can be decomposed as follows:

$$F_{hyd}(t) = \rho C_s(h(t))U^2(t) + \rho C_m(h(t))\dot{U}(t), \tag{16}$$

where C_s is the so-called slamming coefficient, $h(t) = \int_0^t U(\tau)\ \mathrm{d}\tau$ is the penetration depth and C_m is the added mass coefficient. The validity of this decomposition has been assessed by Seng [29] and Sun et al. [30] who performed high-fidelity numerical simulations of rigid bodies entering water at constant and non-constant velocity using state-of-the-art computational fluid dynamics (CFD) approaches. The two-dimensional analytical model proposed by Tassin et al. [31] for the water entry and exit of a body whose shape varies in time suggests that the force acting on a deformable body may be decomposed as follows:

$$F_{hyd}(t) = F_s(\partial D_t, \dot{\partial} D_t) + F_m(\partial D_t, \ddot{\partial} D_t), \tag{17}$$

where the slamming force, F_s, depends on the position, ∂D_t, and the velocity, $\dot{\partial} D_t$, of the body surface in contact with the water and the added-mass reaction force F_m depends on the position, ∂D_t, and the acceleration, $\ddot{\partial} D_t$, of the body surface in contact with the water. Here D_t represents the position of the material domain with respect to the initial position of the free surface. If we now assume that the body shape of a pseudo-rigid body entering the water at a nearly constant speed, U, is only subject to small perturbations with respect to the rigid body position and that these perturbations can be decomposed using the first natural modes of the elastic body, the hydrodynamic force may be decomposed as follows:

$$F_{hyd}(t) \approx F_s(Ut, U, \dot{a}_i(t)) + F_m(Ut, \ddot{a}_i(t)), \tag{18}$$

where coefficients a_i represent the modal coordinates. The added-mass term F_m has the form of an inertial term which may be expressed as follows:

$$F_m(Ut, \ddot{a}_i(t)) \approx \sum_{i=1}^{N} m_i^a(t)\ddot{a}_i(t), \tag{19}$$

where the modal added-mass terms $m_i^a(t)$ evolves in time because the wetted surface of the body evolves as the body enters the water. Note that modal added-mass coefficients m_i^a are equal to zero at the first instant of contact with the water and that they tend to a constant $m_i^a(\infty)$ once the wetted surface stops expanding. This happens when an air cavity starts forming behind the body [see *e.g.* 30]. Substituting Eqs. (18) and (19) into Eq. (11), one obtains:

$$F_s(Ut, U, \dot{a}_i(t)) \approx F_{meas}(t) + \sum_{i=1}^{N} [\alpha_i + \beta_i(t)]\gamma_i(t). \tag{20}$$

Eq. (20) may be used to improve the measurement of the slamming force during pseudo-rigid constant-velocity water-entry experiments. In the context of wave-impact experiments on a pseudo-rigid body, the fluid velocity field in the incoming wave is inhomogeneous and varies in time. In that case, the slamming force obtained with Eq. (20) will be an estimate of the wave excitation force acting on a rigid body, *i.e.* with the contribution of the solid inertia and the added-mass force induced by the response of the structure removed from the original force measurement. The accuracy of the slamming force measurement using this approach will depend on our ability to estimate $\beta_i(t)$ accurately. This point will be illustrated in Sections 3.3 and 3.4. Although the added-mass may be difficult to estimate in some applications, the effect of the added mass may be minimized by designing the experimental set-up adequately. The slamming force estimate may also be affected by the modal velocity terms which appear in the left-hand side of Eq. (20). With the proposed method, it is not possible to compensate for the perturbations which may derive from these terms. However, for small-amplitude high-frequency vibrations, one may speculate that the magnitude of these perturbations is smaller than the ones induced by the inertia terms. These two aspects are discussed in Appendix A where we analyze the relative contributions of the different terms of the hydrodynamic force for a rigid parabolic impactor connected to a linear spring. This simple example shows that, for a given natural frequency of the oscillator, the effect of the added mass decreases as the mass (and the stiffness) of the body increases. This example also confirms that the perturbations of the slamming force induced by the variations of the impactor velocity are much smaller than those induced by the added-mass force. This idea is also supported by the good experimental results obtained in Section 3 below for a case study significantly affected by the added mass.

3. First case study: hydrofoil impacting a calm water surface at constant speed

In this section, we apply the methodology presented in Section 2 to the measurement of the hydrodynamic force during the water entry of a hydrofoil in an initially calm water tank. The experimental set-up is briefly described in Section 3.1 below. The results obtained by performing the identification of the α_i coefficients in air and assuming that $\beta_i(t) = 0$ are presented in Section 3.2. In Section 3.3 we investigate the effect of the water added mass by performing the identification of $(\alpha_i + \beta_i(\infty))$ in the late stage of the impact when the lower part of the mock-up is fully wet. Finally, in Section 3.4, we show that it is possible to obtain satisfactory results by assuming that the $\beta_i(t)$ coefficients evolve linearly in time from the instant of first contact with the water ($t = 0$) to the instant when the mock-up is fully wet ($t = t_{sep}$).

3.1. Experimental set-up

Fig. 2 below shows a picture of the set-up used to conduct the experiments. The hydrofoil is fixed to a six degree-of-freedom motion generator (Mistral 800-type hexapod) which is used to impose a vertical motion during the experiments. The experiments presented here were conducted with the hydrofoil in horizontal position (pitch angle equal to 0°). The force acting on the hydrofoil is measured by a six-component piezo-electric load-cell (Kistler type 9306A31) which connects the hydrofoil to the mast, as shown in Fig. 3(a). The hydrofoil is manufactured from an aluminium alloy block and its shape is based on a NACA0028 profile (see drawing in Appendix B). The chord is equal to 15 cm and the span is equal to 44 cm. The vertical axis of the load cell is located in the vertical plane of symmetry, normal to the chord line and 64 mm behind the leading edge (Fig. 3(b)). Two accelerometers, A_1 and A_2, are located along the line of maximum thickness on both sides of the hydrofoil at a distance of 10 mm of each tip of the hydrofoil. A third accelerometer, A_3, is located in the plane of symmetry behind the load cell. A fourth accelerometer was also fixed to the platform of the hexapod (lower black part in Fig. 2) in order to record the acceleration of the hexapod. The direction of sensitivity of the four accelerometers is parallel to the direction of the F_z component. When performing the experiments, the hydrofoil is accelerated smoothly until it reaches the target velocity U_{max}. The target velocity is reached when the bottom of the hydrofoil is 10 cm above the free surface and the velocity remains constant until the penetration depth is equal to 6 cm. Then the body decelerates and goes up again. The time evolution of the theoretical acceleration and of the acceleration signal measured with the accelerometer fixed to the platform of the hexapod during the two experiments considered here are depicted in Fig. 4 below. These examples correspond to a target impact velocity of 0.6 m/s and 0.4 m/s, respectively. Note that the theoretical and measured signals have been shifted in time such that the impact occurs at t=0 s. One can clearly see that the measured acceleration signal becomes very noisy as soon as the hexapod reaches a certain velocity. The vertical force component and the accelerations measured on the model during the experiments at 0.6 m/s and 0.4 m/s are plotted in Figs. 5 and 6, respectively. The signals denoted γ_1, γ_2 and γ_3 correspond to the signals recorded from accelerometers A_1, A_2 and A_3, respectively. One can clearly see in Fig. 5 that the model is vibrating during the constant velocity stage prior to the impact and that the force is affected by these vibrations. The amplitude of the vibrations increases suddenly at the beginning of the impact due to the fast rise of the hydrodynamic force which occurs at this moment and decreases smoothly afterwards. For the 0.4 m/s experiment, the amplitude of the vibrations with respect to the magnitude of the hydrodynamic force is so high that we can hardly distinguish the hydrodynamic force in Fig. 6. However, it is clear that the amplitude of the vibrations increases significantly after the impact and that the force signal becomes much more oscillatory after flow separation occurs ($t > 0.025$ s). See Hascoët et al. [32] for a detailed description of the hydrodynamic phenomena occurring during the water entry of a foil. The amplitude spectra obtained from a sample of the force and acceleration signals from $t = -0.125$ s to $t = -0.025$ s are depicted in Fig. 7 below together with the amplitude spectrum of the acceleration recorded on the platform of the hexapod, $\gamma_{hexapod}$. One can see that the frequency content is rather different from one experiment to the other. At 0.6 m/s, the force signal is mainly affected by low frequencies (under 200 Hz) and higher frequencies with two peaks around 600 Hz and 700 Hz. The peak with the highest amplitude around 700 Hz corresponds to a natural mode of the model which is clearly visible in Fig. 8 which depicts the amplitude spectra computed from the signals of a hammer test during which the top of the model was impacted on one side (rather close to the line of maximum thickness). Note however that the force signal is not much affected by the vibrations of the hexapod around 800 Hz. In contrast, the main response of the structure during the experiment at 0.4 m/s is concentrated in a narrower bandwidth just below 600 Hz where most of the energy of the hexapod acceleration signal is located. This suggests that the structure responds differently to the excitation of the hexapod in the two experiments conducted at different speeds. Given the frequency content of the signals and the number of accelerometers fixed to the hydrofoil, the analysis has been restricted to the frequencies under 900 Hz. This means that the force and acceleration signals have been low-pass filtered with a cut-off frequency of 900 Hz before applying the procedure described in Sections 3.2–3.4. Hence, it will be assumed that the signals presented in these sections have been low-pass filtered using a Fourier filter with a cut-off frequency f_c=900 Hz when not mentioned otherwise. As the reconstruction methodology is applied to the component F_z, the force measured by the load cell will be referred to as F_z instead of F_{meas} in Sections 3.2–3.4 hereafter.

3.2. Dry-mode identification during the constant velocity stage

Let us consider the two water impact experiments described previously in Section 3.1 and perform a dry-mode identification of the α_i coefficients in Eq. (13) using the signals recorded during the constant velocity stage prior to the impact. For this purpose, we extract a sample of the force signal and of the signals recorded by the three accelerometers fixed to the model corresponding to -0.125 s $< t < -0.025$ s and find the α_i coefficients which minimize the cost function ϵ (see Eq. (14)). A close-up view of

Fig. 2. General view of the experimental set-up.

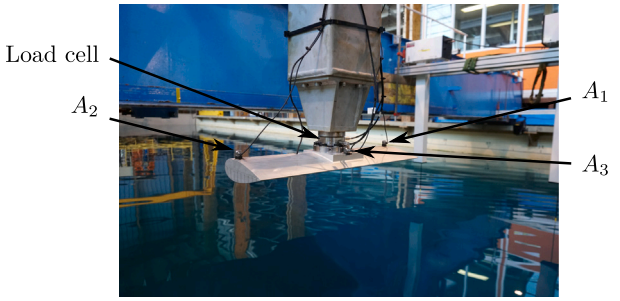

(a) Close-up view of the hydrofoil and its instrumentation: accelerometers A_1, A_2 and A_3 and load cell

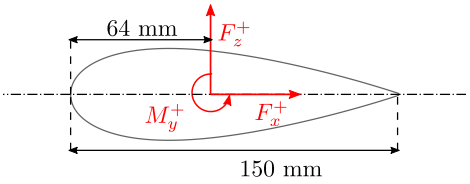

(b) Definition of the force and moment components

Fig. 3. Experimental set-up used to perform the hydrofoil water impact experiments.

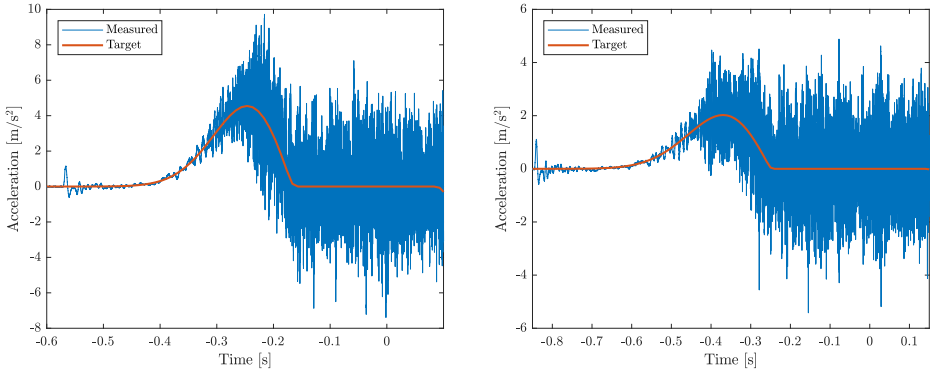

(a) During an experiment at 0.6 m/s (b) During an experiment at 0.4 m/s

Fig. 4. Target and measured acceleration of the hexapod platform.

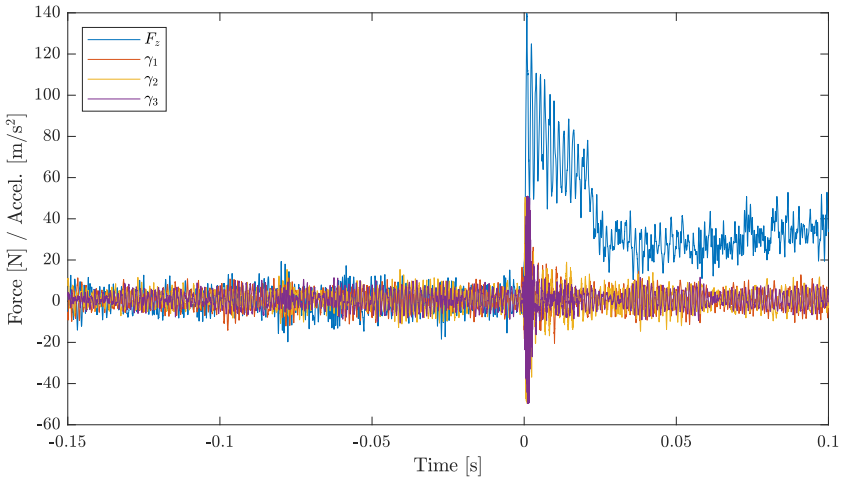

Fig. 5. Force and acceleration raw measurements during an impact at 0.6 m/s.

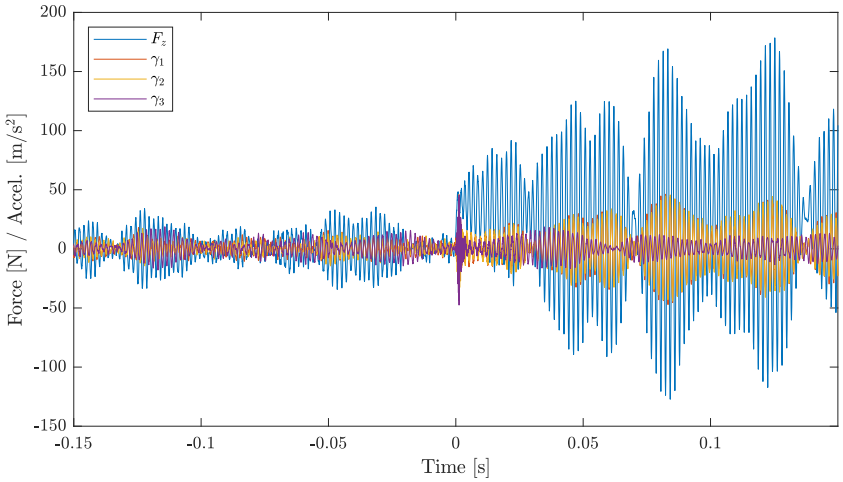

Fig. 6. Force and acceleration raw measurements during an impact at 0.4 m/s.

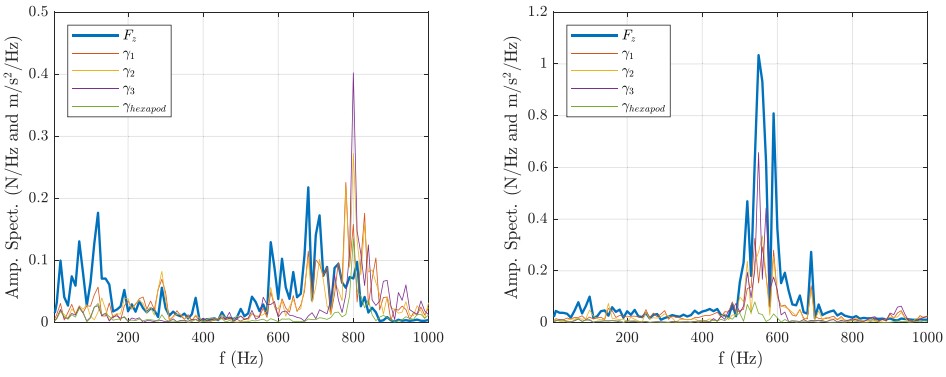

(a) During an experiment at 0.6 m/s (b) During an experiment at 0.4 m/s

Fig. 7. Amplitude spectra of the vertical force and acceleration signals during the constant velocity stage prior to the impact (-0.125 s $< t < -0.025$ s).

the signals used for the identification of the 0.6 m/s experiment is depicted in Fig. 9 below. One can see that there is no obvious correlation between the force signal and one particular acceleration signal. In fact, the signals from the two accelerometers located

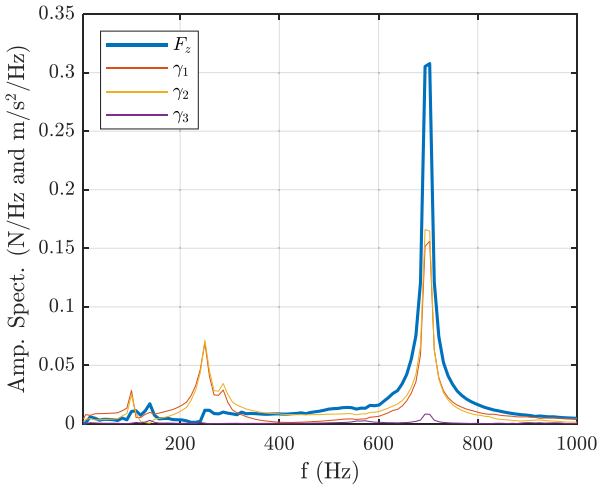

Fig. 8. Amplitude spectra of the vertical force and acceleration signals obtained from a hammer test.

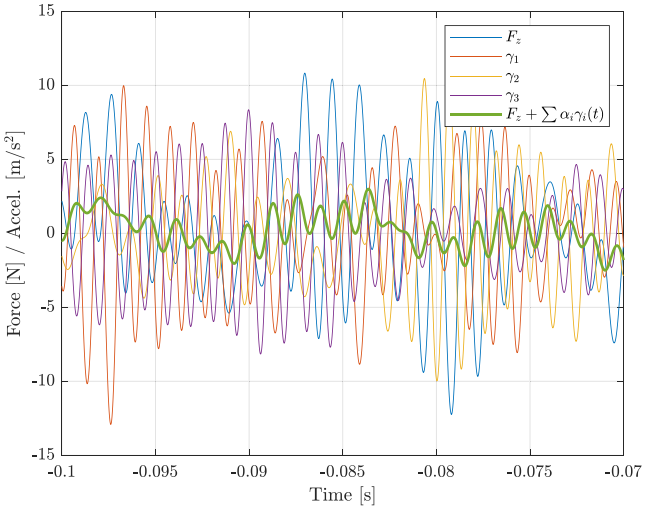

Fig. 9. Force and acceleration signals (filtered at 900 Hz) prior to an impact at 0.6 m/s (during the constant velocity stage).

symmetrically on both sides of the model (γ_1 and γ_2) are clearly not in phase, which shows that both sides of the model respond differently. However, the reconstructed signal denoted $F_z + \sum \alpha_i \gamma_i$ obtained by combining the three acceleration signals to the force signal exhibits a much lower level of oscillations than the original signal F_z. The hydrodynamic impact force obtained using the identified coefficients and the full time series of the signals is depicted in Fig. 10(a) together with the original force signal (filtered at 900 Hz). Similarly to the results obtained with a classical low-pass filter with a lower cut-off frequency f_c of 400 Hz, the reconstructed force is almost free of high-frequency oscillations while retaining all the frequency content of interest in the hydrodynamic force. In Fig. 10(b) which displays a close-up view of the same signals during the early stage of the impact, one can clearly see the advantages of the proposed methodology compared to low-pass filtering the measurement with a lower cut-off frequency. In particular, the signal obtained by low-pass filtering the measurements at 400 Hz exhibits residual low-frequency oscillations prior to the impact which are not visible in the original and reconstructed signals. Also, the low pass filtered signal has a much longer rise time than the other two signals.

The hydrodynamic force obtained with this method for the experiment conducted at 0.4 m/s is depicted in Fig. 11 below together with the (filtered) original force signals. One can see that the reconstruction method performs well before the impact and during the early stage of the impact, but the reconstructed signal remains very oscillatory after the separation occurs ($t > 0.025$ s). Nevertheless, a clear reduction of the oscillations is observed in the reconstructed force signal compared to the original signal. This suggests that the reconstruction method is working well but that the modal-masses are underestimated, which is consistent with an increasing added-mass effect as the body enters the water. Furthermore, given that the ratio between the lineic mass of the hydrofoil and the two-dimensional added-mass obtained by the Wagner model when the hydrofoil is fully wet is $m^* \approx 1.32$, the conclusions of

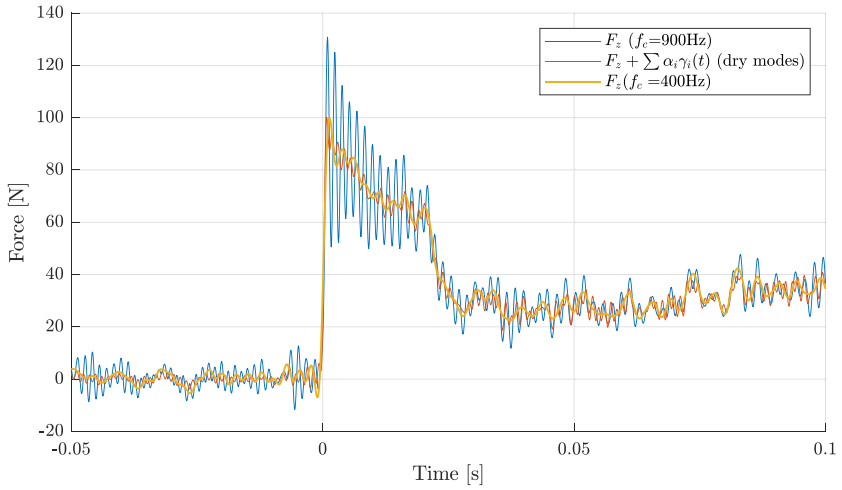

(a) During the whole water impact

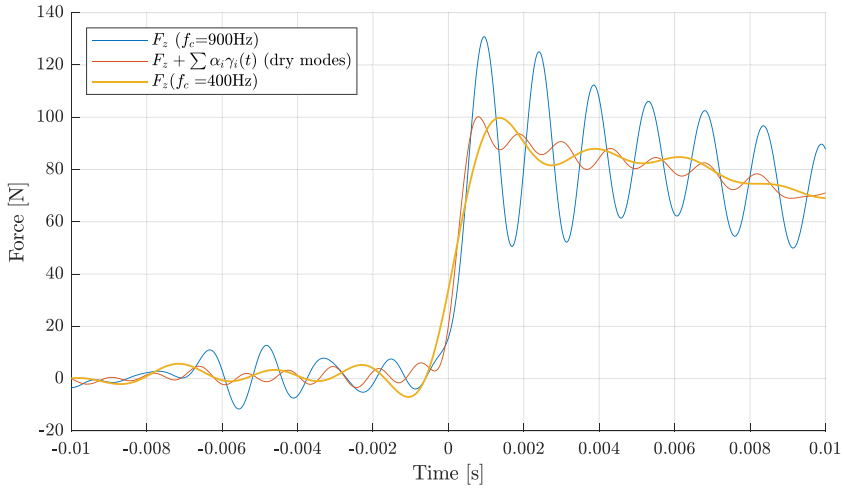

(b) During the early stage of the impact

Fig. 10. Original force measurement and reconstructed hydrodynamic force as a function of time during a water impact at 0.6 m/s.

the theoretical example presented in Appendix A suggest that the added-mass is likely to affect the hydrodynamic force rather significantly.

3.3. Wet-mode identification after separation

As it can be seen in Figs. 10 and 11, the slamming force increases smoothly after separation while the frequencies of the oscillations remain very high. Therefore, the slamming force may be removed from the force measurement by filtering the signal with a high-pass filter (detrending) and a wet-mode identification may be performed. The results obtained by correcting the force measurements with the $(\alpha_i + \beta_i(\infty))$ coefficients identified from t=0.05 s and t=0.1 s with a high-pass cut-off frequency of 100 Hz are depicted in Figs. 12 and 13. One can see that the oscillations have been reduced in the late impact stage. However, the level of the residual oscillations obtained with the wet-mode coefficients prior to the impact is higher than that obtained previously with the dry-mode coefficients. This is more remarkable for the 0.4 m/s case depicted in Fig. 13. Better results may therefore be obtained with β_i coefficients evolving in time as the added-mass increases, as shown in the next section.

3.4. Mixed-mode approach

Ideally, functions $\beta_i(t)$ should evolve in time similarly to the added-mass. Given that the wetted surface width of a two-dimensional blunt body (*e.g.* parabola) evolves as the square root of the time during an impact at constant speed and that the

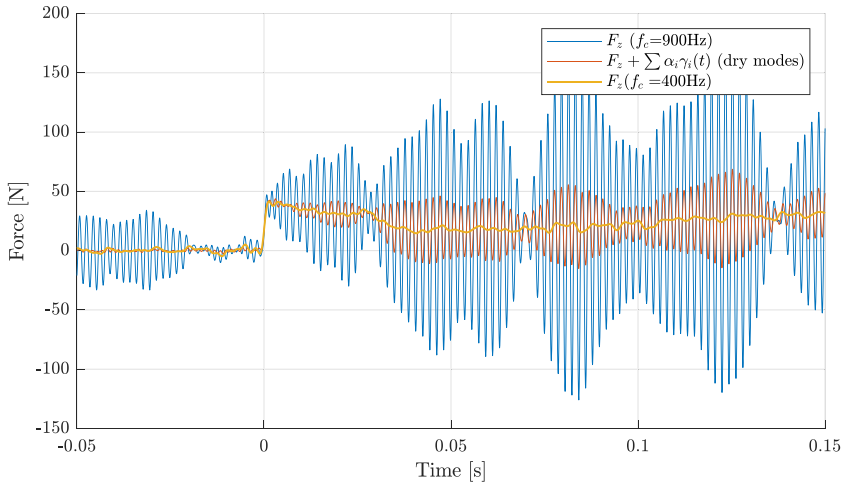

Fig. 11. Original force measurement and reconstructed hydrodynamic force during a water impact at 0.4 m/s.

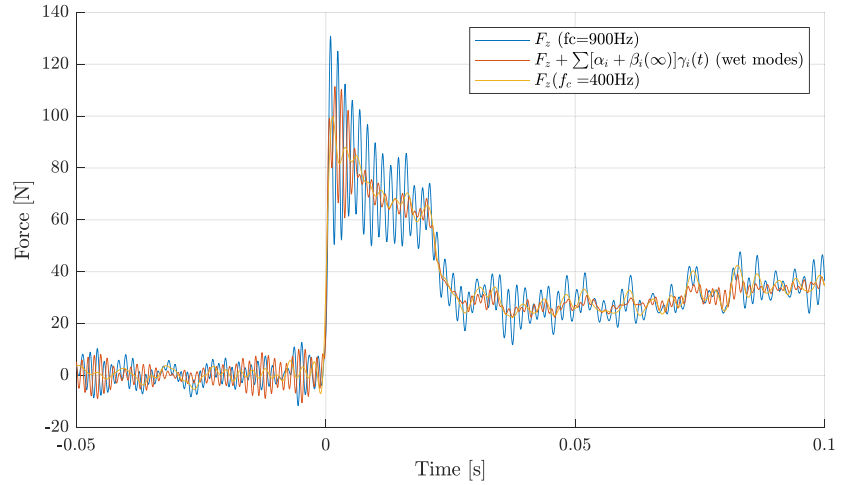

Fig. 12. Original force measurement and reconstructed hydrodynamic force during a water impact at 0.6 m/s with a wet-mode identification.

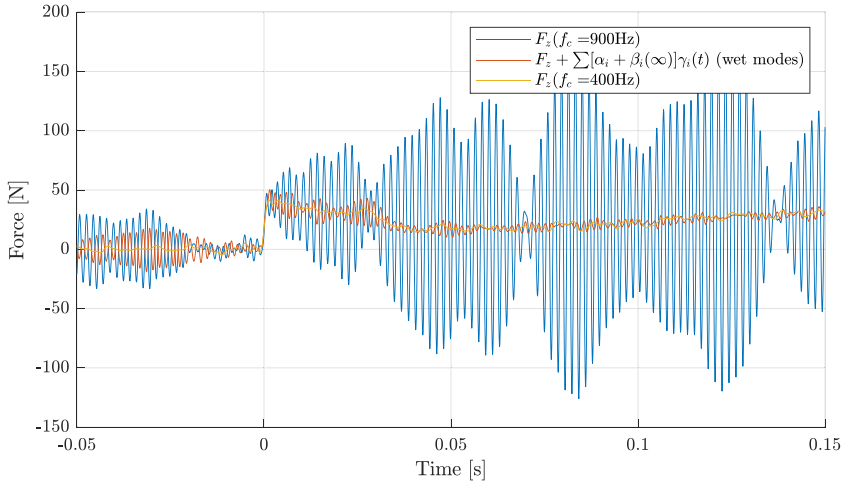

Fig. 13. Original force measurement and reconstructed hydrodynamic force during a water impact at 0.4 m/s with a wet-mode identification.

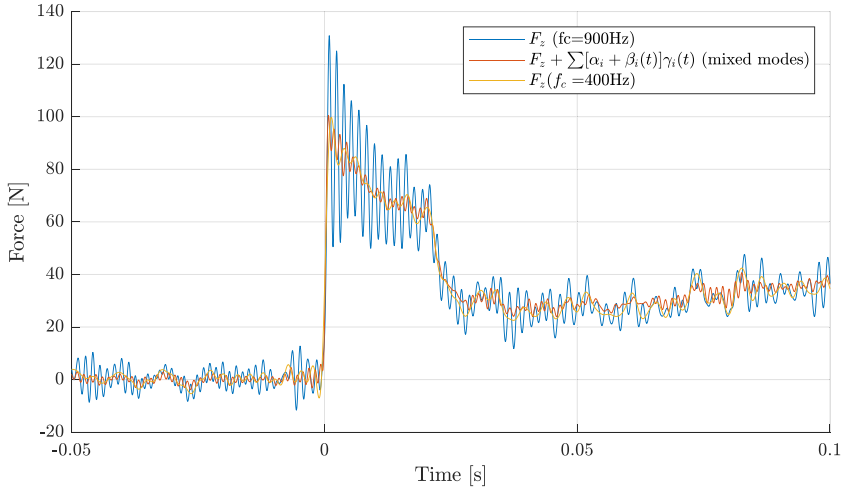

Fig. 14. Original force measurement and reconstructed hydrodynamic force during a water impact at 0.6 m/s with a mixed-mode approach.

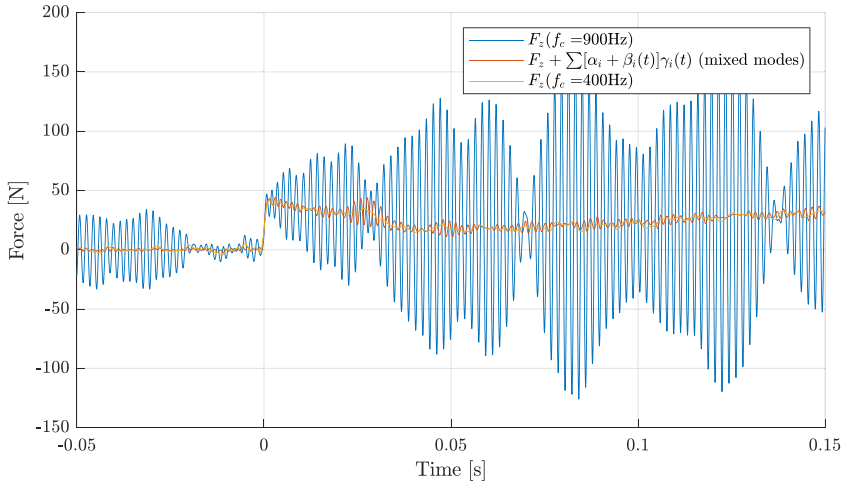

Fig. 15. Original force measurement and reconstructed hydrodynamic force during a water impact at 0.4 m/s with a mixed-mode approach.

added-mass evolves as the square of the wetted-surface width (see Appendix A), reasonably good results may be obtained by enforcing a linear evolution of functions $\beta_i(t)$ between the first instant of impact (t=0 s) and the time instant of separation (t_{sep}=0.025 s): $\beta_i(0 < t < t_{sep}) = \beta_i(\infty) \cdot t/t_{sep}$ and $\beta_i(t > t_{sep}) = \beta_i(\infty)$. The results obtained by this approach are depicted in Figs. 14 and 15. One can see that the results obtained by interpolating linearly the α_i coefficients (denoted "mixed modes") preserve the advantages of the dry-mode identification in the early stage of impact and of the wet-mode identification in the late stage of the impact without adding additional noise in between. The efficiency of the approach for the 0.4 m/s case is remarkable given the poor signal-to-noise ratio of the original measurement.

4. Second case study: breaking wave impacting a segmented vertical circular cylinder

In this section, we apply the methodology presented in Section 2 to the measurement of the hydrodynamic force acting on a sub-structure of a segmented vertical cylinder during a breaking-wave impact event. The experimental set-up is briefly described in Section 4.1. The identification procedure, which is based on hammer tests, is presented in Section 4.2. In Section 4.3, the accuracy of the reconstruction method is first assessed trough comparisons between the reconstructed force and the force measured by the instrumented hammer. In Section 4.4, the methodology is finally applied to the reconstruction of the hydrodynamic forces recorded during two breaking-wave impacts displaying different levels of vibration.

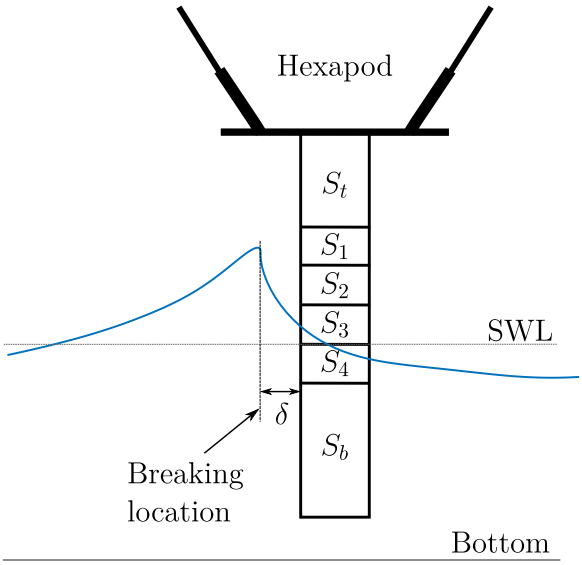

Fig. 16. Description of the experimental set-up. The parameter δ corresponds to the distance between the front face of the cylinder and the breaking location. The horizontal dotted line represents the position of the still water level (SWL).

4.1. Experimental set-up

The experimental set-up described in Fig. 16 was designed in order to measure the hydrodynamic loads acting on a vertical cylinder during long-crested breaking-wave impact events. The cylinder is 1.8 m high and has a diameter of 0.4 m. It is fixed to a hexapod used to control the position of the mock-up. The hexapod itself is fixed to a hanging frame placed on the rails situated along the wave flume. The experiments were conducted in the wave flume of Ifremer, in Plouzané, France. The flume is 2 m deep, 4 m wide and 40.5 m long. It is equipped with a piston-type wave maker and an absorbing beach.

As depicted in Figs. 16 and 17(a), the cylinder is composed of six sections, out of which four are instrumented with multi-component load cells. The instrumented sections, denoted S_1, S_2, S_3 and S_4, are located close to the still water surface with the aim of measuring locally the hydrodynamic force distribution exerted by the breaking waves on these 15 cm high substructures. Each instrumented section is composed of an outer part, an inner part and a load cell, as shown in Fig. 17(b) which displays an exploded view of an instrumented section. The inner parts are made of stainless steel and the outer parts of aluminium alloy. The inner parts of the different sections are screwed to each other to form the so-called backbone of the cylinder. Each outer part is connected to its inner part via the load cell. The outer parts form the skin of the mock-up. The load measured on a load cell thus corresponds to the load acting on the outer part. The three instrumented upper sections S_1, S_2 and S_3 are equipped with MCS10-025 type HBM load cells having a 5 kN nominal range in the horizontal directions. Section S_4 is equipped with a MCS10-010 type HBM load cell with a 2 kN nominal range in the horizontal directions. A gap of 3 mm was left between the different skin elements in order to avoid any risk of contact during the experiments. This gap was sealed with surgical tape to ensure watertightness between the sections. It was assumed that the surgical tape had a negligible mechanical rigidity.

The results presented in the sequel correspond to the upper instrumented section (S_1). However, the proposed methodology has also been applied to the second section (S_2), which was also subject to vibrations during the experiments. The mock-up was initially designed such as to minimize the effect of the backbone response on the force measurements. The stiffness of the load cells and the mass of the skin elements were also taken into consideration in the design to ensure a sufficiently high natural frequency of the spring–mass system which they form together. Despite these efforts, it was observed during a first experimental campaign that the skin elements themself responded elastically to the breaking-wave impact loads. Six accelerometers were then fixed to the skin elements in order to implement the proposed reconstruction methodology. Our analysis focuses on the measurement of the horizontal component of the hydrodynamic force corresponding to the wave propagation direction, F_{hyd}, from the force component measured by the load cell in the same direction, F_{meas}. The distribution of the accelerometers is shown in Fig. 18. Note that the accelerometers fixed on the skin (A_1 to A_5) are placed about two centimeters above the bottom of the section. The choice of the location of the accelerometers has been guided by Finite Element Analyses (FEA) of the skin elements. FEA makes it possible to compute the shapes and frequencies of the first natural modes. The results obtained by FEA assuming that the central part of the skin element is supported by a linear spring representing the load cell elasticity are detailed in Appendix C (the elasticity of the backbone is neglected in these simulations). Several accelerometer distributions were tested and the final distribution was found after observing experimentally the spectra of the signals recorded by the different accelerometers and the load cell during the hammer tests. This made it possible to correlate the sensitivity of a particular accelerometer to the different modes which are affecting the load cell. On the contrary, as the load cell is not sensitive to some particular modes (*e.g.* the torsion mode), the location and

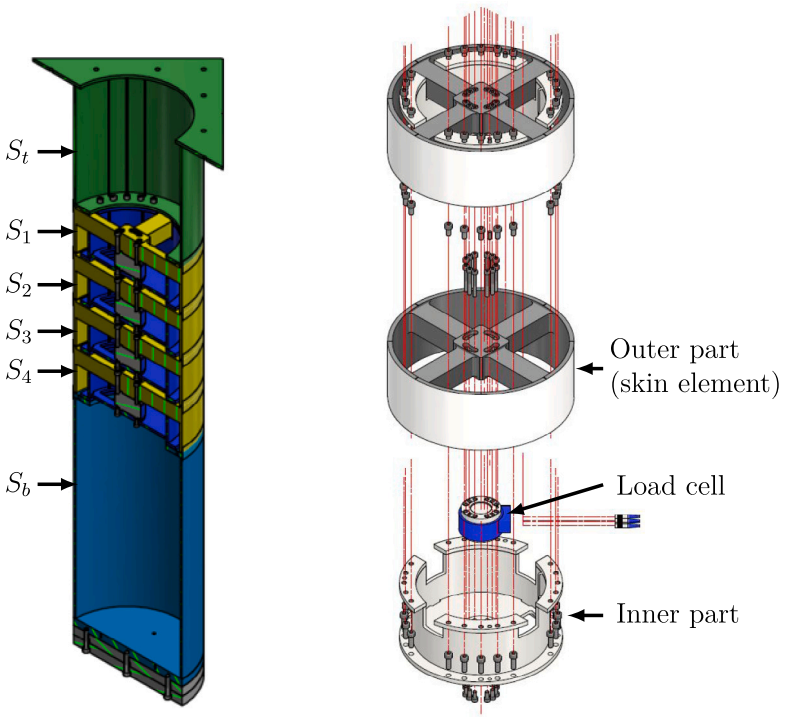

(a) Cross-sectional view of the mockup (b) Exploded view of two instrumented sections

Fig. 17. Description of the mockup.

orientation of the accelerometers was set such as to minimize their sensitivity to these modes. The accelerometers labeled A_1 to A_5 located on the skin are mainly used to capture the vibrations induced by the three-dimensional elastic deformations of the skin element while the central accelerometer A_6 is mainly used to capture the "rigid-body" motion of the skin. As all the accelerometers are oriented along the radial direction of the cylinder, their sensitivity to the torsion mode (mode 1 in Appendix C) is marginal. The accelerometers labeled A_1 to A_5 are piezoelectric charge accelerometers of types Brüel and Kjær 4370-V and 4381-V. They were plugged to charge amplifiers of types Kistler 5167 A and 5165 A. The selected amplification range allowed to measure accelerations up to 200 g. Accelerometer A_6 is an integrated electronics piezoelectric (IEPE) sensor of type Kistler 8640A50 with a nominal range of 50 g. The accelerometers were glued to the mock-up using epoxy and cyanoacrylate adhesive.

The breaking waves were generated through the focalization of a JONSWAP spectrum with a significant height of 0.15 m, a peak period of 2.25s and a peak enhancement factor of 3.3 truncated at 0.8 Hz (frequencies above 0.8 Hz are neglected). With these parameters, the altitude of the crest estimated numerically with a fully nonlinear potential flow solver is equal to 0.40 m when the breaking starts (when the tangent to the free surface becomes locally vertical).- The theoretical focus location was adjusted iteratively by means of fully nonlinear potential flow simulations in order to enforce the breaking location to be at the desired location. The distance between the mock-up and the wavemaker was chosen so as to enforce a certain distance, δ (see Fig. 16), between the front face of the cylinder and the breaking location. Note that the magnitude of the impact force, and as a consequence the magnitude of the vibrations that it induces, is strongly dependent on that parameter δ.

4.2. Identification of the reconstruction coefficients through hammer tests

The identification of the α_i coefficients was performed following a hammer test approach which consisted in impacting the outer part of the section in a direction as close as possible to the wave propagation direction (x-direction) with an instrumented hammer (Kistler type 9724A5000). The position of the mock-up during the identification procedure was similar to the one of the mock-up during the experiments (as described in Fig. 16). The force signals measured by the impact hammer and the load cell of S_1 during a hammer test on section S_1 are depicted in Fig. 19(a) together with the acceleration signals γ_1, γ_2 and γ_3 measured by accelerometers A_1, A_2 and A_3, respectively. A zoomed-in view of these signals close to the impact is shown in Fig. 19(b). The signals are centered by subtracting their mean value during a period of 0.2 s before the impact. All the signals are low-pass filtered using a Fourier filter with a cut-off frequency of $f_c = 1040$ Hz to remove the high-frequency noise and the high-frequency vibrations that are not compensated for due to the finite number of accelerometers. The time interval of the signals used for the coefficient identification is delimited by the two black vertical lines shown in Fig. 19(a). The beginning of this interval corresponds to the instant at which

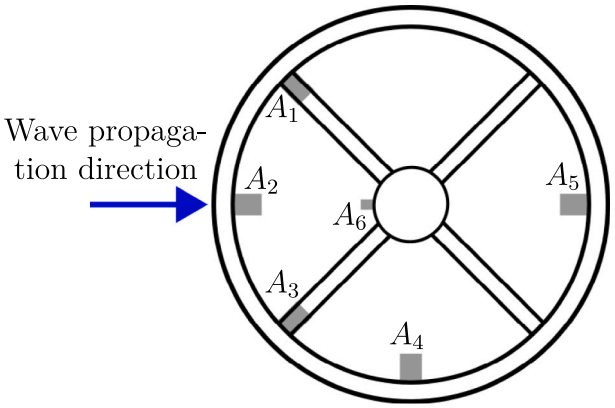

Fig. 18. Top-view of a skin element and distribution of the accelerometers A_i.

the hammer signal is back to zero. The length of this time interval is 0.1 s. The α_i coefficients are obtained by minimizing the cost function ϵ defined in Eq. (14). All six accelerometers are used for the identification and the reconstruction. The Fourier transforms of the force signals measured by the load cell and the hammer signal are depicted in Fig. 20 along with the Fourier transforms of the different accelerometer signals. One can see that the response of the structure affects significantly the force signal recorded by the load cell. The numerical results presented in Appendix C are in accordance with the presence of several natural frequencies in the considered bandwidth, although some of the natural frequencies predicted numerically differ rather significantly from the experimental observation. In particular, it seems that the experimental value for the frequency of modes 2 and 3 is closer to 140 Hz than the value of 241 Hz predicted numerically. This difference might come from a coupling effect between the skin element and the backbone. Note that mode 1, which corresponds to a torsion mode around the z-axis, is hardly visible in the force and acceleration signals. Also note that the computation of the mode shapes helped finding an appropriate arrangement for the accelerometers, but the mode shapes predicted numerically were not used in the identification of the reconstruction coefficients α_i.

4.3. Reconstruction of a hammer impulse force

In order to assess the accuracy of the force reconstruction method, let us consider the force signal recorded by the hammer during a hammer test. Indeed, if the reconstruction methodology works well, it should be able to reconstruct the time evolution of the force impulse exerted by the hammer on the mock-up. The results obtained with the reconstruction methodology denoted $F_{meas} + \sum \alpha_i \gamma_i$ are depicted in Fig. 21(a) together with the force signal recorded with the hammer, F_{ham}, the original measured force signal, F_{meas}, and the result obtained from the low-pass filtering of the load cell measurement with a 300 Hz cut-off frequency. One can see that the reconstruction methodology successfully removes the majority of the oscillations which are present in the original force signal. In addition, the reconstruction method is also able to compensate for the dynamic amplification and the delay of the original force signal obtained from the load cell. In fact, the reconstructed force and the force measured with the hammer almost overlap. The relative difference between the reconstructed force and the force recorded with the hammer in terms of maximum force is under 5%. In comparison to the results obtained with a cut-off frequency of 300 Hz, the prediction of the maximum force is much improved and the level of residual oscillations is significantly lower with the reconstruction method. The Fourier transforms of the different signals are depicted in Fig. 21(b). One can see that the main peaks present in the original load cell measurement are removed with the multimode reconstruction approach. Only small deviations remain between the reconstructed force and the hammer force.

4.4. Wave impact force reconstruction

In this section, the reconstruction methodology is applied to experiments during which breaking waves impact the mock-up. Two different distances between the cylinder and the breaking point are considered: $\delta = 0.36$ m and $\delta = 0.71$ m. In both cases, the reconstruction relies on the α_i coefficients derived from the hammer tests. We first apply the methodology to the case displaying the lowest level of vibrations ($\delta = 0.71$ m), which corresponds to the impact of a fully broken wave. The reconstructed force is depicted in Fig. 22 together with the original force signal and the signal obtained with a 300 Hz cut-off frequency low-pass filter. In that case, a first impact occurs when the tongue of the overturning wave hits the cylinder and a second stronger impact occurs when the "main" wave front reaches the cylinder. One can see in Fig. 22(b) that the mock-up starts vibrating at the first impact and that the amplitude of the vibrations decreases progressively until the second impact occurs, which induces a sudden increase in the vibration amplitude. The Fourier transforms of the different signals are shown in Fig. 23. It appears clearly that the methodology allows to compensate for the oscillations induced by several modes of vibration while keeping the high-frequency content of the signal. Moreover, one can see in Fig. 22(a) ($t > 26.95$ s) that the low-frequency oscillations induced by the vibrations of the beam

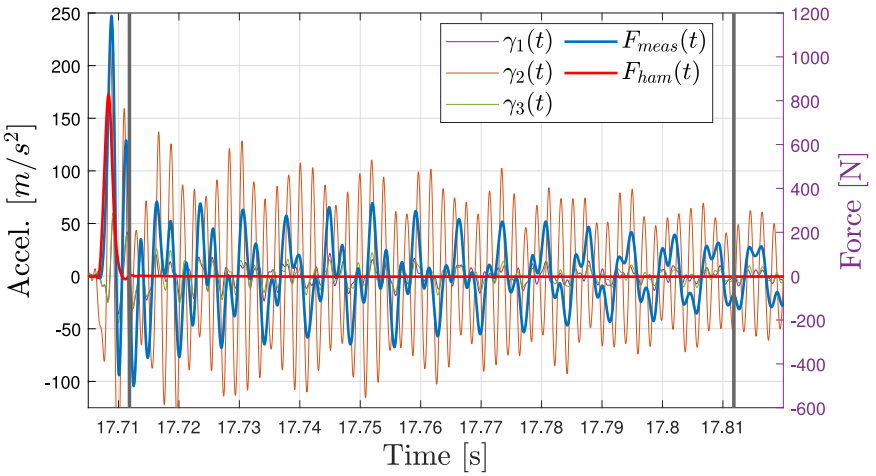

(a) Impact and subsequent vibrations

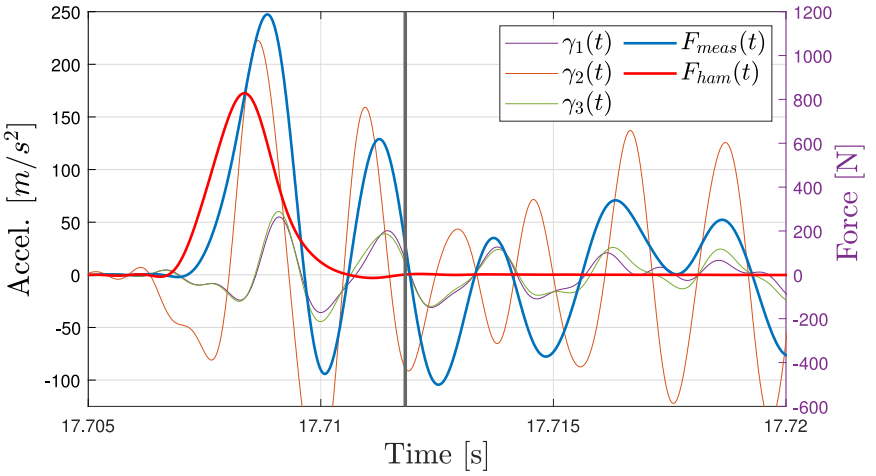

(b) Zoomed-in view at the instant of impact

Fig. 19. Accelerations and forces measured by A_1, A_2, A_3, the load cell of the upper section and the impact hammer. The vertical lines correspond to the limits of the time interval used to identify the α_i coefficients.

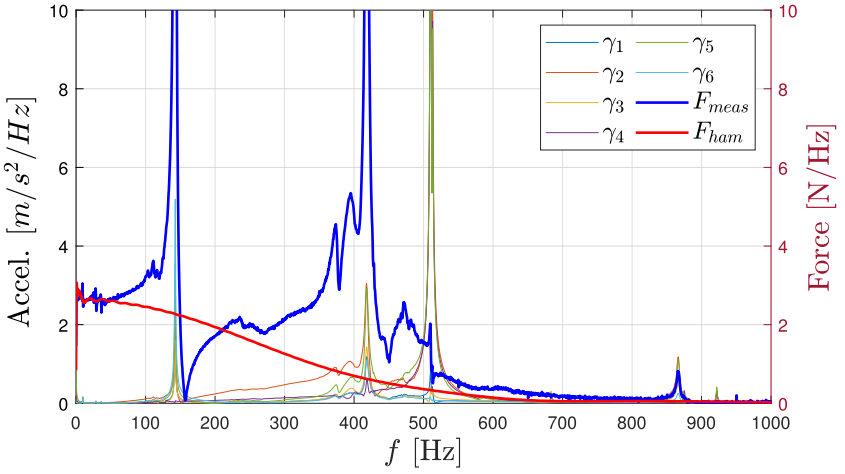

Fig. 20. Fourier transforms of the accelerations measured by the six accelerometers, of the force measured with the load cell F_{meas} and of the force measured with the impact hammer F_{ham}.

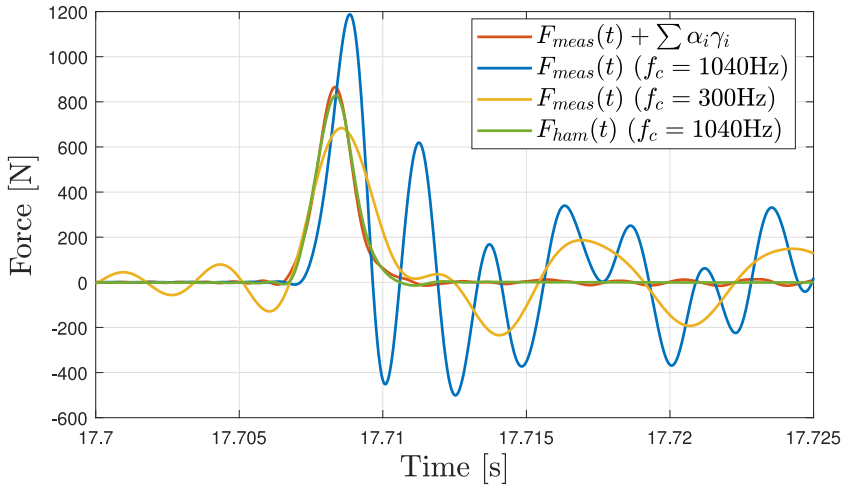

(a) Force evolution as a function of time

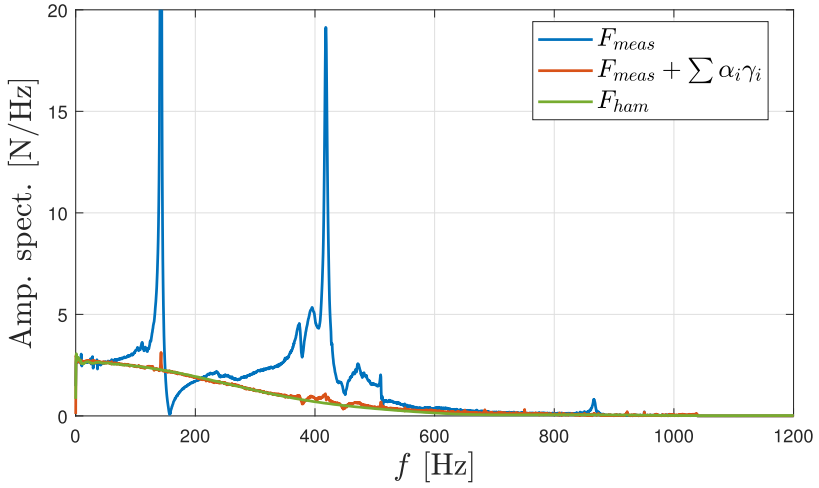

(b) Fourier transforms of the force signals

Fig. 21. Original force measurement on the load cell and reconstructed force during a hammer impact on S_1. For comparison purposes, the force measured by the impact hammer and the 300 Hz low-pass filtered force measured on the load cell are represented.

are also compensated for. This is an important improvement compared to the results obtained using a filter with a 300 Hz cut-off frequency. Hence, in addition to preserving the high-frequency content of the hydrodynamic forcing load, the reconstruction methodology also prevents from the artificial residual low-frequency oscillations which are visible on the results obtained with a 300 Hz cut-off frequency in Fig. 22(b). Let us now consider the second breaking wave impact case corresponding to $\delta = 0.36$ m. The evolution of the force as a function of time obtained from the different approaches is depicted in Fig. 24 and the corresponding amplitude spectra are depicted in Fig. 25. As one can see, the amplitude of the vibrations is much larger during this experiment. Also note that only one impact occurs in that case because the tongue of the wave is less developed when the wave reaches the cylinder. The reconstruction method also performs well in that case: the low-frequency oscillations are well compensated for and an important part of the higher-frequency oscillations are compensated for. After the force peak, some residual oscillations are observed. The spectrum of the compensated load displays oscillations in the frequency band [300 ; 600] Hz. In this frequency band, discrepancies were also observed between the compensated load during a hammer impact and the load recorded with the hammer (see Fig. 21(b)). Adding more accelerometers to the structure may improve the reconstruction, in particular in terms of residual oscillations. However, the accuracy of the force reconstruction may also be affected by the evolution of the added mass during the test. Following the approach described in Section 3.3 where the reconstruction coefficients were identified in the late stage of the impact (wet-mode approach), we have tried to use this approach for the breaking wave impacts, but the results were

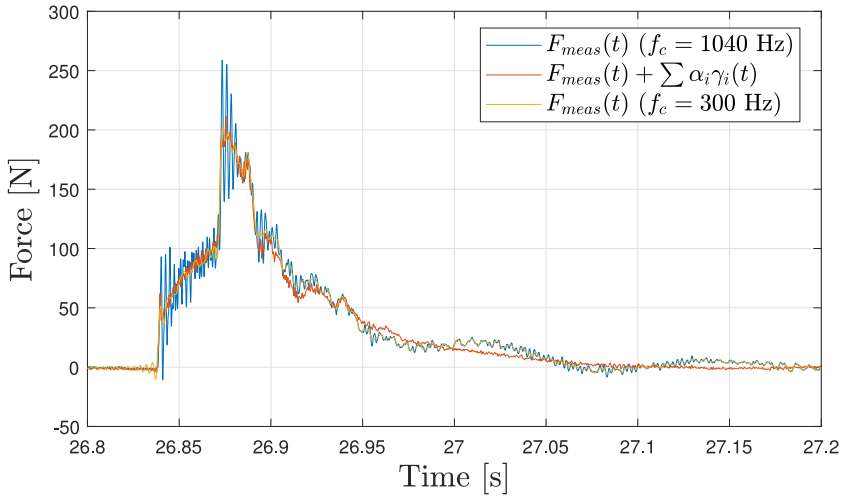

(a) Force evolution

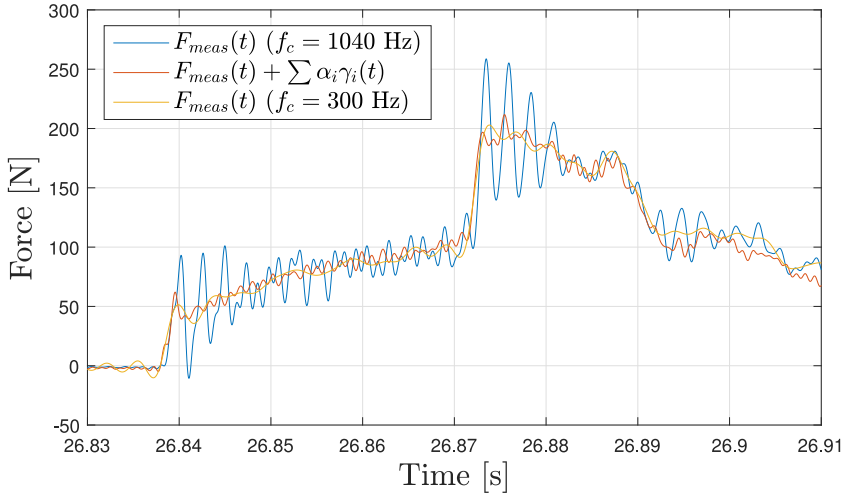

(b) Zoomed-in view on the early stage of impact

Fig. 22. Force evolution as a function of time during a breaking wave impact experiment carried out with $\delta = 0.71$ m.

worse than those obtained with the hammer test approach. One may conclude that the added mas has no significant effect on the reconstruction, but a more likely conclusion is that the portion of signal extracted from the late stage of impact is not adapted to the identification of the reconstruction coefficients. A potential indication of the role played by the added mass may be found in Fig. 26 which shows a comparison of the amplitude spectra of the force signals recorded by the load cell (original signals) during a breaking wave impact and a hammer test. Both spectra have rather similar shapes, but the peaks of the wave impact spectrum seem to be shifted towards lower frequencies. This observation is consistent with an increase in the modal mass and may therefore indicate that the rapid increase of the added mass during the experiments may affect the accuracy of the force reconstruction. Unfortunately, as explained above, we were unable to perform a satisfactory identification of the reconstruction coefficients in the late stage of the breaking wave impacts. Taking into account the effect of the added mass remains an open and challenging problem for this kind of experiments. Following the conclusions of the theoretical illustration presented in Appendix A, a solution for decreasing the relative effect of the added mass may consist in increasing the mass of the structure itself, for example by using steel instead of aluminium for the skin part (see Fig. A.30).

5. Conclusion

We have proposed a new method to reduce the effect of the vibrations on the force measurements during water impact experiments conducted with pseudo-rigid bodies. The method consists in recording the response of the structure using several

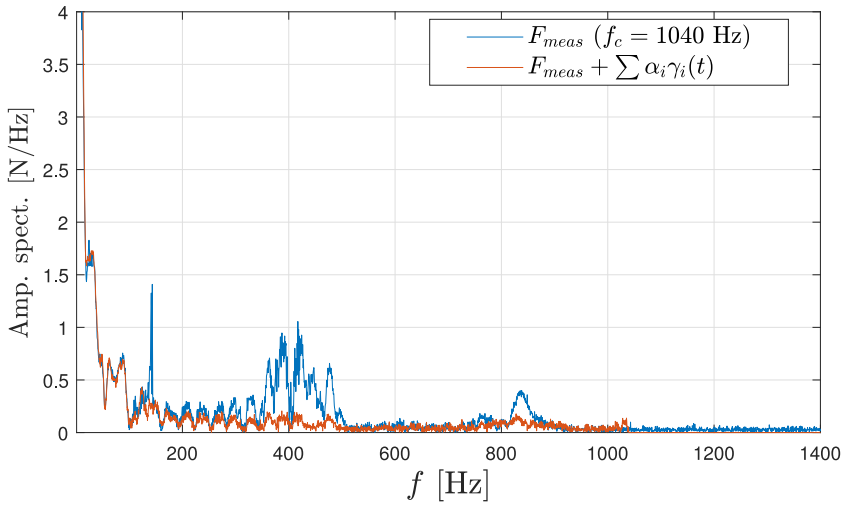

Fig. 23. Fourier transforms of the original and reconstructed force signals depicted in Fig. 22.

accelerometers and to estimate the part of the load cell signal which is due to the response of the structure. Using the principles of momentum conservation, we have shown that it was theoretically possible to recover the hydrodynamic excitation force provided the rate of change of momentum (the inertial term) of the impacting body was known. Following the standard assumption that the body response can be well described by a small set of normal modes, we have shown that it was possible to estimate accurately the inertial term by recording the body acceleration in several locations. The number of accelerometers and their locations should be adapted according to the number of modes and to the shape of the modes which are excited during the experiments. The accuracy of the approach has been demonstrated by studying two different case studies of increasing complexity. We have shown that it was possible to perform the identification of the reconstruction coefficients in different manners. For the hydrofoil test case, we managed to perform the identification using a portion of the signal extracted from the experiment itself. In that case, we managed to perform a dry- and wet-mode identification by selecting appropriate portions of the recorded signals. We also showed that it was possible to interpolate the reconstruction coefficients in time from the dry to the wet mode coefficients in order to model the effect of an increasing added mass during the experiments. For the vertical cylinder test case, the reconstruction coefficients were identified from hammer tests. The use of an instrumented hammer made it possible to accurately assess the accuracy of the reconstruction method through comparisons between the reconstructed force and the impact force recorded with the hammer. This rather complex example which involves truly three-dimensional deformations of a three-dimensional body shows the potential of the approach to deal with complex problems.

We have shown that the proposed method was able to compensate for several modes of vibration. To the best of the authors' knowledge, it is the first time that such a thing is achieved in the field of water impacts. To achieve this, it is helpful to compute the natural modes of the structure, especially in order to distribute the accelerometers appropriately. However, thanks to the identification procedure, there is no need to know accurately the location of the accelerometers and there is no need to model very finely the structure of the mock-up.

One of the difficulties encountered during the experiments is the effect of the added mass. We managed to take into account satisfactorily the evolution of the added mass during the experiments carried out with the hydrofoil, but we did not succeed for the breaking wave impact experiments carried out with the vertical cylinder. Taking into account the effect of the added mass remains an open and challenging problem for this kind of experiments. Adapting the technique used for the hydrofoil poses two difficulties. The first one is to estimate the reconstruction coefficients for the wet modes, which we did not manage to do. One probable reason for this failure is that the frequency content in the late stage was not broad enough compared to the frequency content of the early force impulse. A possible workaround for this task could be to infer the evolution of the modal mass of each mode from the peak shift observed in the force amplitude spectra. Doing so would require identifying the dry modal mass of each mode, which may be achieved using the principal component analysis. The second difficulty is to find a suitable interpolation for the modal masses. Indeed, the linear interpolation suggested for the hydrofoil may not be suited for three-dimensional water impact problems. In the case of the circular cylinder, the flow separates smoothly from the body in the late stage of the impact and an air cavity starts forming. The transition between the dry mode and wet mode regimes may therefore be more difficult to identify than in the case of the hydrofoil because the separation cannot be detected in the force signal.

The difficulties arising from a non-constant added mass could possibly advocate for an increase in the mass and the stiffness of the mock-up so as to reduce the amplitude of the oscillations and the amplitude of the added-mass force, but without changing the

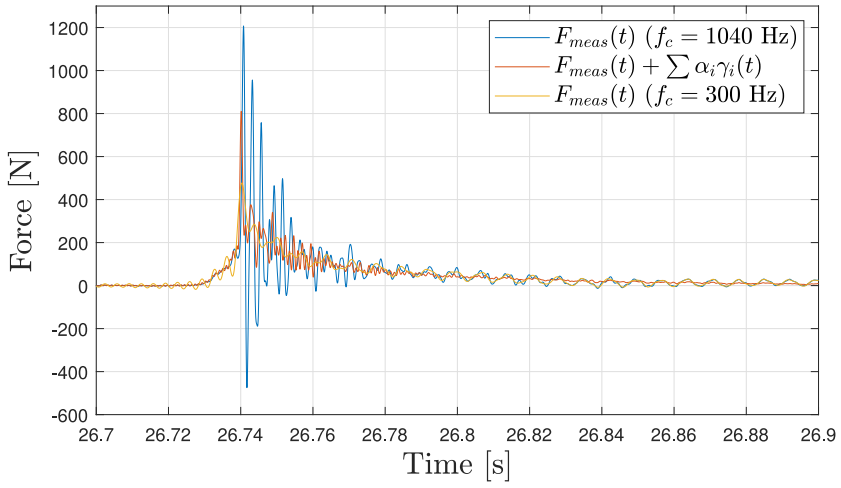

(a) Force evolution

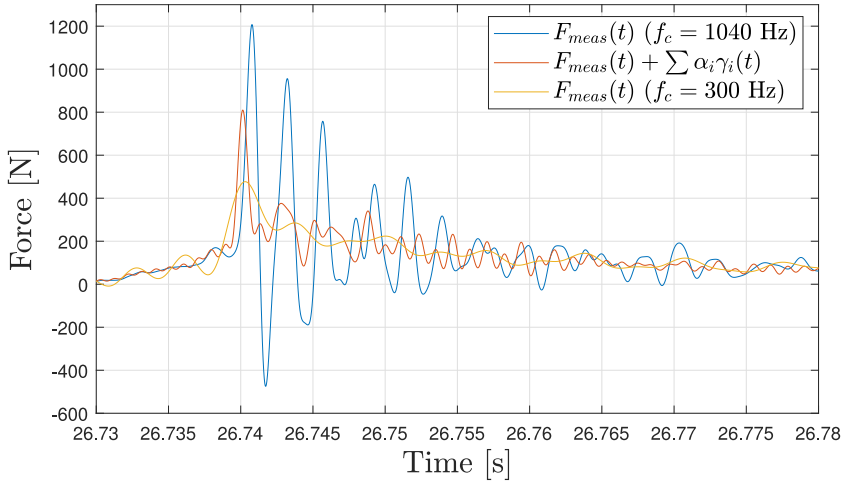

(b) Zoomed-in view at the instant of the peak force

Fig. 24. Force evolution as a function of time during a breaking wave impact experiment carried out with $\delta = 0.36$ m.

natural frequencies of the structure. This idea goes against the standard recommendation of minimizing the mass of the mock-up in order to minimize the perturbations of the force measurements when vibrations occur. In that sense, this method could have an important impact on the design of experimental set-ups for water impact or other types of dynamic problems. The amplitude of the vibrations may also be minimized by adding some extra damping to the structure of the mock-up. An interesting point about the proposed method is that it does not require an accurate identification of the damping properties of the structure. However, in the case of important damping, the amplitude of the vibrations subsequent to a hammer impact decrease very fast and therefore it may be difficult to extract a portion of the signal with a sufficiently large frequency content. In that case, one may prefer performing the identification of the reconstruction coefficients during the impulse rather than after.

It is worth reminding that the method has been implemented on these two test cases without changing the original design of the mock-up. We have shown that it was possible to perform the identification of the reconstruction coefficients without conducting specific tests. Therefore, some experiments carried out by the readers in the past may be re-processed *a posteriori* to correct the force measurements (if accelerometers were present during the experiments).

The method is conceptually simple and trivial to implement from a signal processing point of view, which makes it attractive for potential applications. It is computationally very efficient because the only operations that it requires consist in a simple linear combination of different signals. In addition, the proposed method introduces no delay in the signals, which makes it attractive for real-time and control applications. The main difficulty when implementing this method is finding the right accelerometer arrangement for the particular problem under investigation.

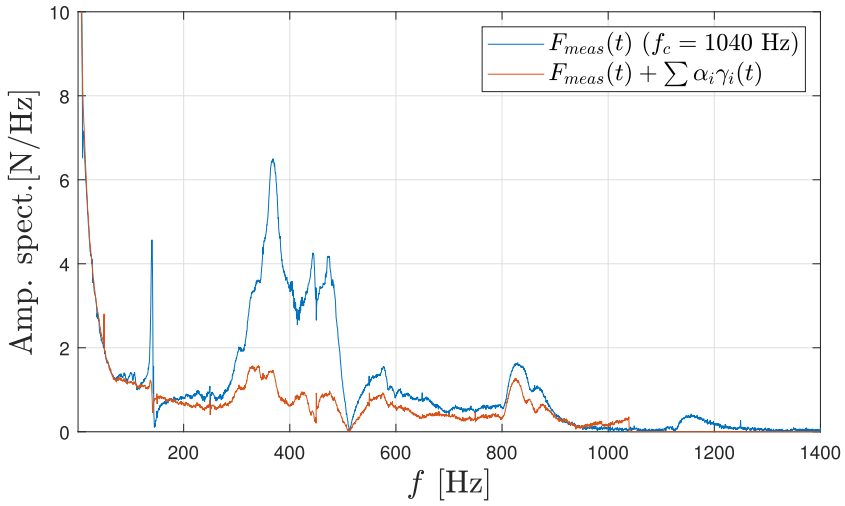

Fig. 25. Fourier transforms of the original force signal and reconstructed force signal plotted in Fig. 24.

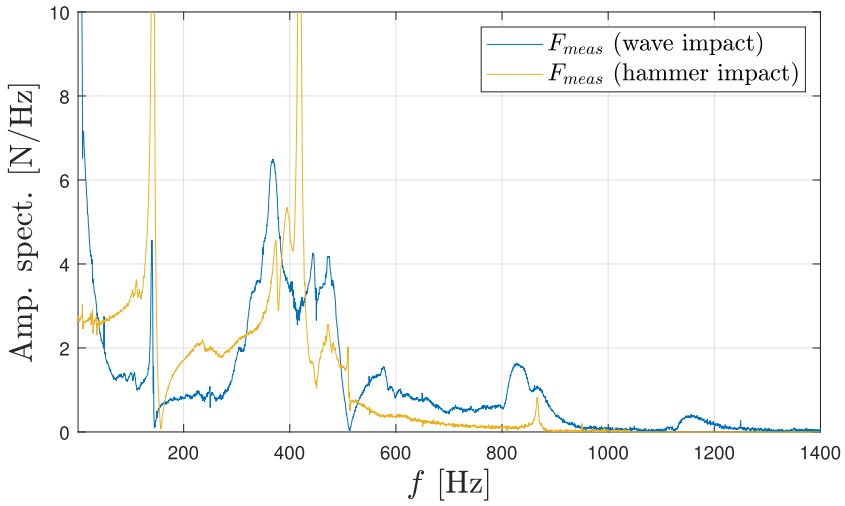

Fig. 26. Comparison of the Fourier transforms of the force signals measured during a wave impact and a hammer impact.

CRediT authorship contribution statement

Alan Tassin: Writing – review & editing, Writing – original draft, Validation, Supervision, Project administration, Methodology, Investigation, Funding acquisition, Formal analysis, Data curation, Conceptualization. **Florian Hulin:** Writing – review & editing, Writing – original draft, Validation, Methodology, Investigation, Formal analysis, Data curation, Conceptualization. **Nicolas Jacques:** Writing – review & editing, Writing – original draft, Validation, Supervision, Project administration, Methodology, Funding acquisition, Formal analysis, Conceptualization.

Declaration of competing interest

The authors declare that they have no known competing financial interests or personal relationships that could have appeared to influence the work reported in this paper.

Data availability

Data will be made available on request.

Acknowledgments

The work presented in Section 3 was supported by the French National Agency for Research (ANR) and the French Government Defense Procurement and Technology Agency (DGA) [ANR-17-ASTR-0026 APPHY]. The work presented in Section 4 benefited from government support managed by the Agence Nationale de la Recherche, France under the program Investissements d'Avenir with the reference ANR-10-IEED-06-34 related to the DIMPACT project. The authors would like to thank Prof. Alexander A. Korobkin and Dr Tatyana Khabakhpasheva from the University of East Anglia, United Kingdom and Dr Marc Prevosto for the discussions on the topic of this paper. Alan Tassin and Florian Hulin would like to thank the technical team of Ifremer's wave tank in Plouzané for their support in designing, setting-up and running the experiments.

Appendix A. Theoretical illustration: hydrodynamic force acting on a rigid parabolic impactor connected to a linear spring

Let us consider a rigid parabolic impactor of mass m connected to a linear spring of stiffness k impacting a calm water surface, as illustrated in Fig. A.27. The spring represents the elasticity of a load cell during a water impact, with $F_{meas} = -k\delta_z(t)$, δ_z being the additional displacement induced by the compression/extension of the spring. The upper end of the spring is assumed to move with a constant velocity $V > 0$. Applying Newton's second law to the rigid impactor, one obtains:

$$-m\ddot{\delta_z}(t) = k\delta_z(t) + F_{hyd}(t), \tag{A.1}$$

with $\delta_z(0) = 0$ and $\dot{\delta_z}(0) = 0$. For the sake of simplicity, we will assume that the hydrodynamic force is equal to the force predicted by the original Wagner model:

$$F_{hyd} = \underbrace{\rho\pi U(t)c(t)\dot{c}(t)}_{F_s} + \underbrace{\rho\frac{\pi}{2}c(t)^2\dot{U}(t)}_{F_m}, \tag{A.2}$$

where $U(t) = V + \dot{\delta_z}$ represents the speed of the rigid impactor and $c(t) = 2\sqrt{h(t)R}$ is the half-width of the wetted surface for a parabolic contour defined by $z = x^2/(2R)$ and a penetration depth $h(t) = Vt + \delta_z$. As one is in general interested in the early stage of the impact, we will assume that the local deadrize angle at $x = c_{max}$ is equal to 30°, c_{max} being the value of the wetted surface half-width reached at the end the simulation. In order to make sure that the mechanical system has enough time to respond to the hydrodynamic excitation force, let us assume that the period of the oscillator is 20 times shorter than the duration of the impact, t_{max}, which gives $\sqrt{k/m} = 20 \times 2\pi/t_{max}$. The force results obtained by solving Eq. (A.1) for different values of $m^* = m/(\rho\pi c_{max}^2/2)$ are depicted in Figs. A.28–A.30. Parameter m^* corresponds to the ratio between the mass of the body and the liquid added-mass at the end of the simulations ($t = t_{max}$). Note that the different force results are non-dimensionalized with respect to the theoretical slamming force, $2\pi\rho RV^2$, predicted by the Wagner model for a water impact at constant speed (*i.e.* in absence of body vibrations). One can see in Fig. A.28 that the values of the measured force, F_{meas}, obtained for the different values of m^* are rather close to each other at the beginning of the impact and that the response of the spring–mass system leads to a maximum force value almost about two times larger than the theoretical constant speed slamming force. Note that the oscillations of F_{meas} decrease during the impact for $m^* = 1$ because the oscillations of the rigid body are damped by the slamming force. At the end of the impact, the oscillations of the measured force are smaller for $m^* = 1$ than for the higher values. However, the hydrodynamic force results depicted in Fig. A.29 show that the hydrodynamic force obtained with the heaviest impactor ($m^* = 10$) is the closest to the theoretical slamming force, meaning that the fluctuations of the hydrodynamic force caused by the vibrations of the impactor are the smallest in this case. The relative difference between the slamming force and the theoretical constant speed slamming force is depicted in Fig. A.30 together with the non-dimensional added-mass force. We can see that the amplitude of the added-mass force oscillations are much larger than the deviation of the slamming force from the theoretical constant speed slamming force. The maximum values of $|F_s - (2\pi R\rho V^2)|/(2\pi R\rho V^2)$ equal to 1.6%, 0.53% and 0.16% for $m^* = 1$, 3 and 10, respectively. Note that the added-mass coefficient can be approximated by the theoretical constant speed added-mass with a maximum error $|\delta_z|/(Vt)$ of 0.57%, 0.19% and 0.058% for $m^* = 1$, 3 and 10, respectively. However, when the added-mass is difficult to estimate, the effect of

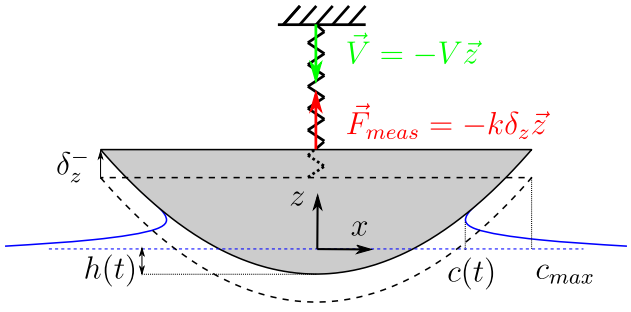

Fig. A.27. Rigid parabolic body connected to a linear spring impacting a calm water surface at constant speed $V > 0$.

the added-mass on the hydrodynamic force may be reduced by choosing a heavier body rather than a lighter body with a similar "dry" natural frequency. For a deformable body, this could suggest using steel rather than an aluminium alloy to manufacture the model because steel is heavier than aluminium while both materials have similar Young modulus to density ratios.

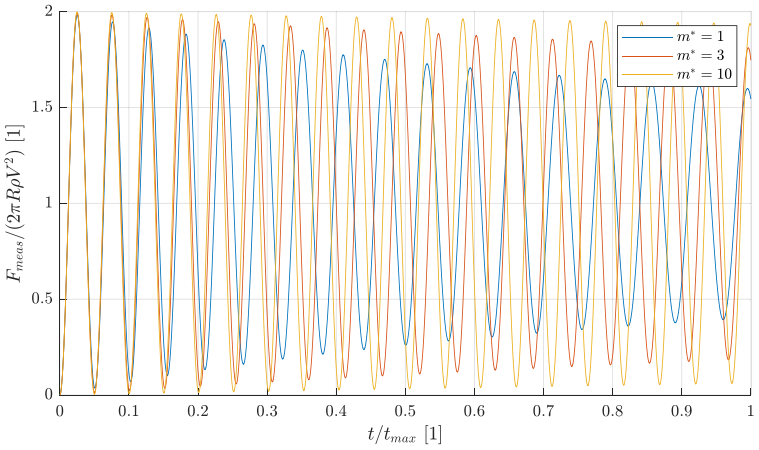

Fig. A.28. Non-dimensional measured force $F_{meas}/(2\pi R\rho V^2)$ as a function of the non-dimensional time t/t_{max}.

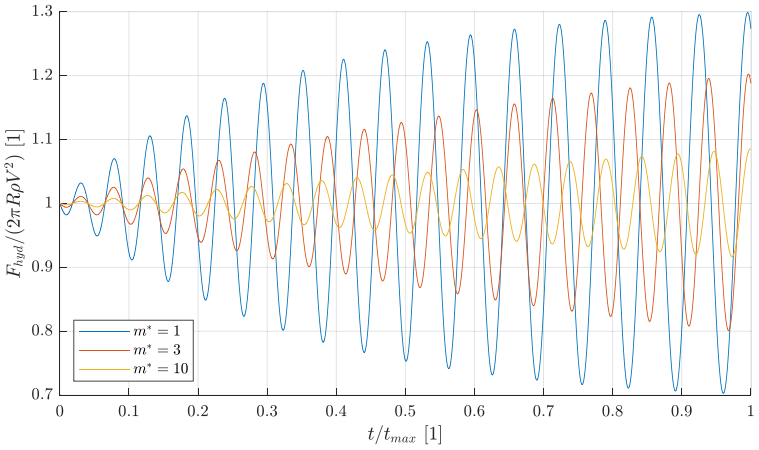

Fig. A.29. Non-dimensional hydrodynamic force $F_{hyd}/(2\pi R\rho V^2)$ as a function of the non-dimensional time t/t_{max}.

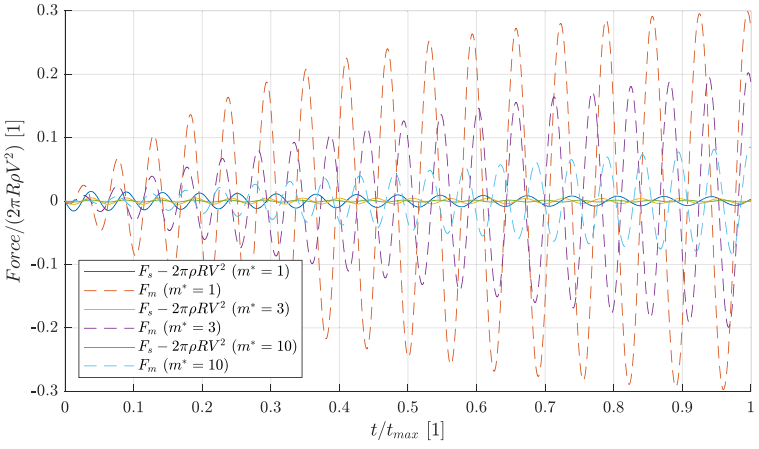

Fig. A.30. Relative difference between the slamming force and the theoretical constant velocity slamming force, $[F_s - (2\pi R\rho V^2)]/(2\pi R\rho V^2)$, and non-dimensional added-mass force $F_m/(2\pi R\rho V^2)$ as a function of the non-dimensional time t/t_{max}.

Appendix B. Detailed drawing of the hydrofoil mock-up

See Fig. B.31.

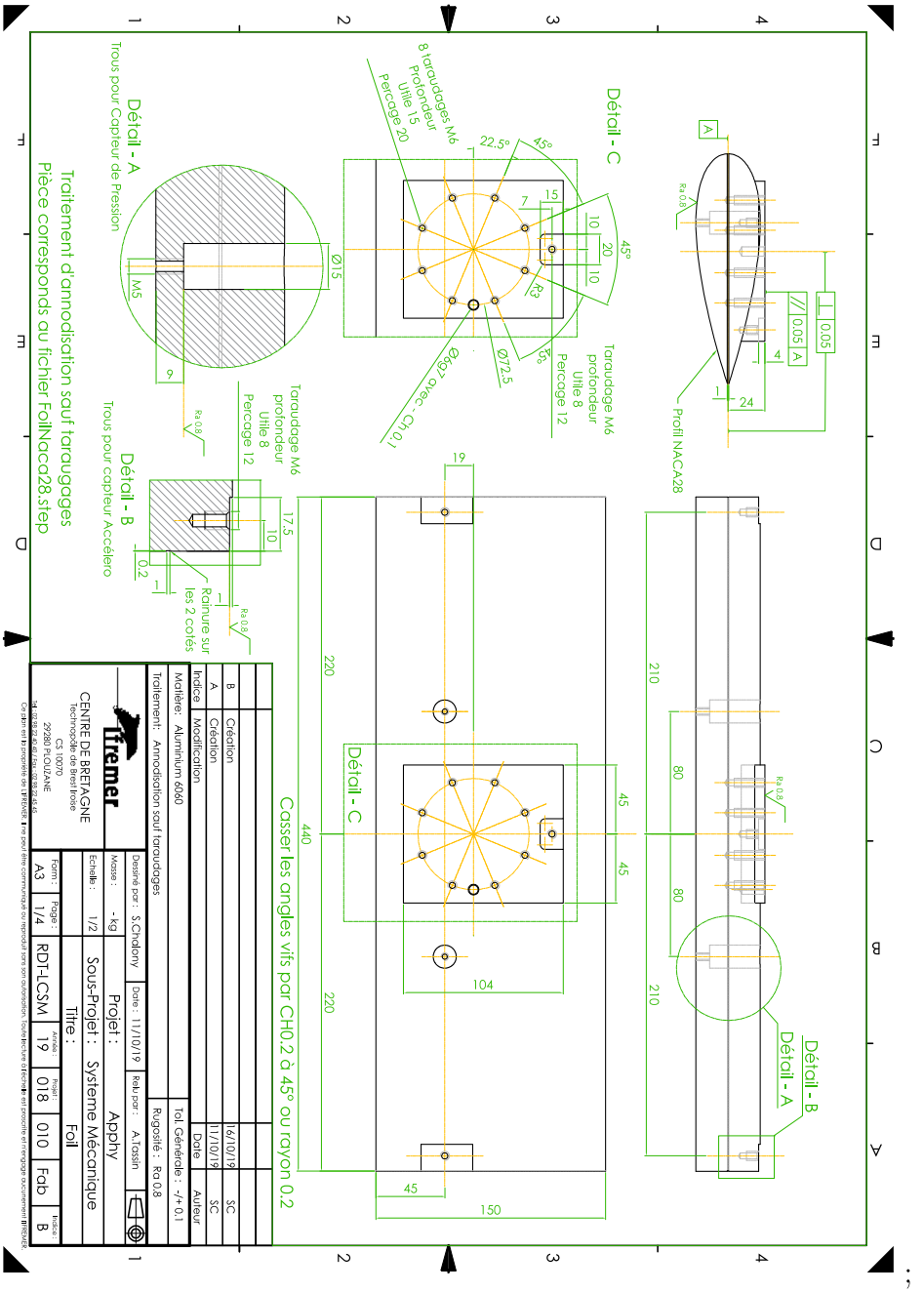

Fig. B.31. Detailed drawing of the hydrofoil mock-up.

Appendix C. Natural modes of the skin section computed numerically

A finite element analysis of the outer part of the section was carried out to determine the shape and frequencies of the first natural modes of the section. A linear spring boundary condition was assigned to the skin part in order to take into account the elasticity of the load cell but the elasticity of the backbone was neglected. The shapes of the different modes are depicted in Fig. C.32. The natural frequencies of the modes are given in the caption.

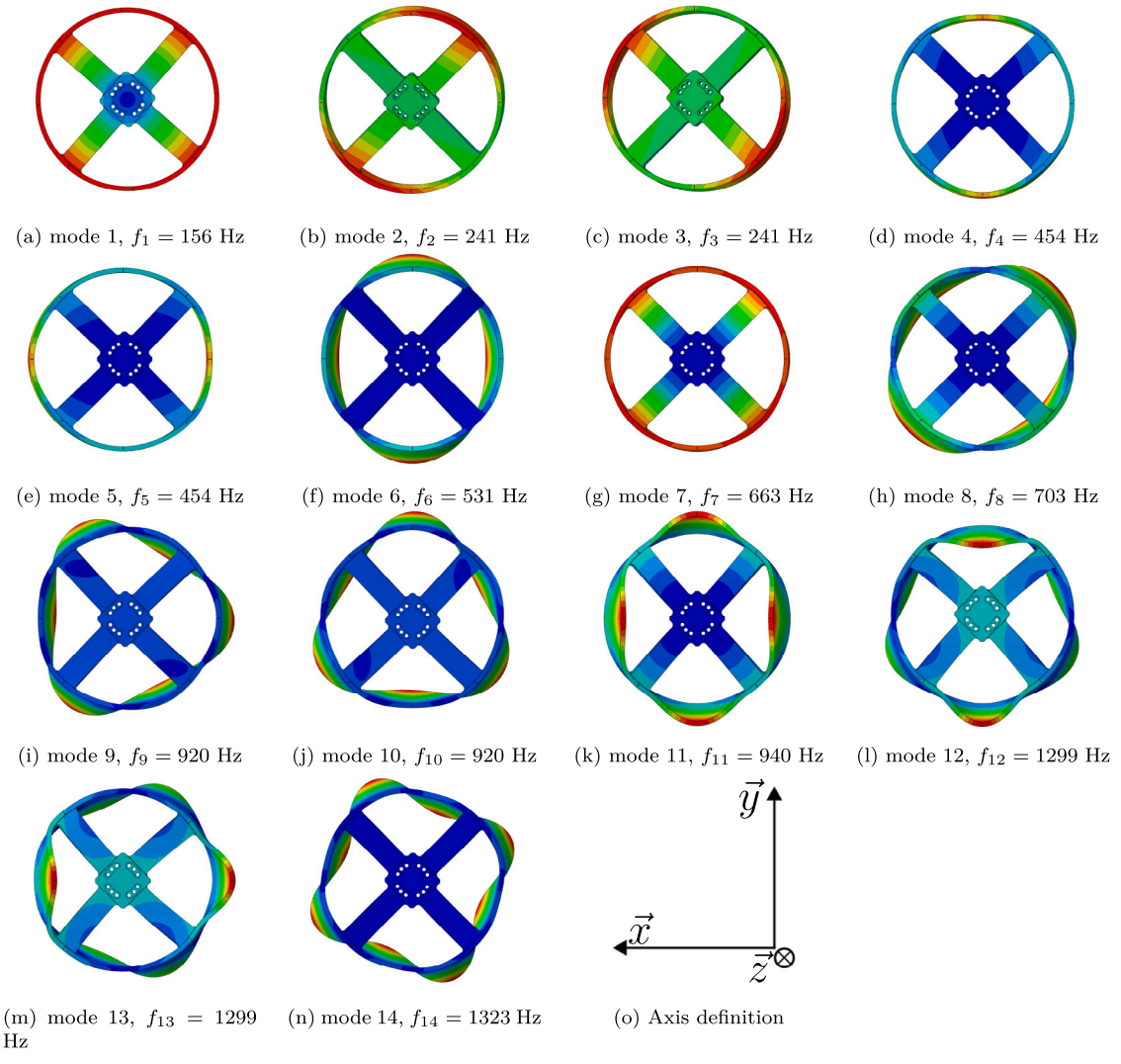

Fig. C.32. Top-view of the shape of the different modes of the outer section with a linear spring boundary condition at its center.

References

[1] J. de Lauzon, Q. Derbanne, Š. Malenica, Slamming induced whipping computations on a large database of container ships, in: T. Okada, K. Suzuki, Y. Kawamura (Eds.), Practical Design of Ships and Other Floating Structures, Springer, Singapore, 2021, pp. 857–877, http://dx.doi.org/10.1007/978-981-15-4624-2_52.

[2] J.-H. Kim, Y. Kim, R.-H. Yuck, D.-Y. Lee, Comparison of slamming and whipping loads by fully coupled hydroelastic analysis and experimental measurement, J. Fluid. Struct. 52 (2015) 145–165, http://dx.doi.org/10.1016/j.jfluidstructs.2014.10.011.

[3] S. Hallowell, A. Myers, S. Arwade, Variability of breaking wave characteristics and impact loads on offshore wind turbines supported by monopiles, Wind Energy 19 (2) (2016) 301–312, http://dx.doi.org/10.1002/we.1833.

[4] A. Antonini, J.M.W. Brownjohn, D. Dassanayake, A. Raby, J. Bassit, A. Pappas, D. D'Ayala, A Bayesian inverse dynamic approach for impulsive wave loading reconstruction: Theory, laboratory and field application, Coast. Eng. 168 (2021) 103920, http://dx.doi.org/10.1016/j.coastaleng.2021.103920.

[5] A. Alsalah, D. Holloway, M. Mousavi, J. Lavroff, Identification of wave impacts and separation of responses using EMD, Mech. Syst. Signal Pr. 151 (2021) 107385, http://dx.doi.org/10.1016/j.ymssp.2020.107385.

[6] I.M.C. Campbell, P.A. Weynberg, Measurement of Parameters Affecting Slamming, Technical Report 440, University of Southampton, Wolfson Unit for Marine Technology, 1980, Technology Reports Centre No. OT-R-8042.
[7] A.H. Moalemi, H. Bredmose, A. Ghadirian, T. Kristiansen, Cylinder water entry on a perturbed water surface, J. Fluid Mech. 965 (2023) A16, http://dx.doi.org/10.1017/jfm.2023.403.
[8] A. Tassin, N. Jacques, A. El Malki Alaoui, A. Nême, B. Leblé, Hydrodynamic loads during water impact of three-dimensional solids: Modelling and experiments, J. Fluid. Struct. 28 (2012) 211–231, http://dx.doi.org/10.1016/j.jfluidstructs.2011.06.012.
[9] T. Breton, A. Tassin, N. Jacques, Experimental investigation of the water entry and/or exit of axisymmetric bodies, J. Fluid Mech. 901 (2020) A37, http://dx.doi.org/10.1017/jfm.2020.559.
[10] E. Spinosa, A. Iafrati, A noise reduction method for force measurements in water entry experiments based on the Ensemble Empirical Mode Decomposition, Mech. Syst. Signal Pr. 168 (2022) 108659, http://dx.doi.org/10.1016/j.ymssp.2021.108659.
[11] A. Iafrati, S. Grizzi, Cavitation and ventilation modalities during ditching, Phys. Fluids 31 (5) (2019) 052101, http://dx.doi.org/10.1063/1.5092559.
[12] A. Iafrati, S. Grizzi, M. Siemann, L. Montañés Benítez, High-speed ditching of a flat plate: Experimental data and uncertainty assessment, J. Fluid. Struct. 55 (2015) 501–525, http://dx.doi.org/10.1016/j.jfluidstructs.2015.03.019.
[13] P. Vega-Martínez, J. Rodríguez-Rodríguez, T. Khabakhpasheva, A. Korobkin, Hydro-elastic effects during the fast lifting of a disc from a water surface, J. Fluid Mech. 869 (2019) 726–751, http://dx.doi.org/10.1017/jfm.2019.208.
[14] L. Diebold, E. Baudin, Bureau Veritas sloshing model tests & CFD calculations for ISOPE sloshing benchmark, in: The Twenty-Fourth International Ocean and Polar Engineering Conference, OnePetro, 2014, ISOPE-I-14-463, ISBN: 978-1-880653-91-3.
[15] O. Kimmoun, A. Ratouis, L. Brosset, Sloshing and scaling: experimental study in a wave canal at two different scales, in: The Twentieth International Offshore and Polar Engineering Conference, OnePetro, 2010, ISOPE-I-10-185.
[16] J. Wienke, H. Oumeraci, Breaking wave impact force on a vertical and inclined slender pile—theoretical and large-scale model investigations, Coast. Eng. 52 (5) (2005) 435–462, http://dx.doi.org/10.1016/j.coastaleng.2004.12.008.
[17] S. Wang, T. Larsen, H. Bredmose, Experimental and numerical investigation of a jacket structure subject to steep and breaking regular waves, Mar. Struct. 72 (2020) 102744, http://dx.doi.org/10.1016/j.marstruc.2020.102744.
[18] E.J. de Ridder, T. Bunnik, J.M. Peeringa, B.T. Paulsen, C. Wehmeyer, P. Gujer, E. Asp, Summary of the joint industry project wave impact on fixed foundations (WIFI JIP), in: International Conference on Offshore Mechanics and Arctic Engineering, Vol. 57786, ASME, 2017, http://dx.doi.org/10.1115/OMAE2017-62040, V010T09A081.
[19] L. Suja-Thauvin, J.R. Krokstad, E.E. Bachynski, E.-J. de Ridder, Experimental results of a multimode monopile offshore wind turbine support structure subjected to steep and breaking irregular waves, Ocean Eng. 146 (2017) 339–351, http://dx.doi.org/10.1016/j.oceaneng.2017.09.024.
[20] R. Clough, J. Penzien, Dynamics of Structures, third ed., Computers & Structures, Inc, California, 2003.
[21] A. Korobkin, T. Khabakhpasheva, S. Malenica, Hydrodynamic pressure in hydroelastic impact problems, in: 36^{Th} International Workshop on Water Waves and Floating Bodies, 2021, 25-28 April 2021, Seoul, Korea (Virtual).
[22] S.-J. Choi, K.-H. Lee, O.T. Gudmestad, The effect of dynamic amplification due to a structure's vibration on breaking wave impact, Ocean Eng. 96 (2015) 8–20, http://dx.doi.org/10.1016/j.oceaneng.2014.11.012.
[23] K. Maes, W. Weijtjens, E.-J. de Ridder, G. Lombaert, Inverse estimation of breaking wave loads on monopile wind turbines, Ocean Eng. 163 (2018) 544–554, http://dx.doi.org/10.1016/j.oceaneng.2018.05.049.
[24] A. El Malki Alaoui, A. Nême, A. Tassin, N. Jacques, Experimental study of slamming coefficients during vertical water entry of axisymmetric rigid shapes at constant speeds, Appl. Ocean Res. 37 (2012) 183–197, http://dx.doi.org/10.1016/j.apor.2012.05.007.
[25] M. Found, I. Howard, A. Paran, Interpretation of signals from dropweight impact tests, Compos. Struct. 42 (4) (1998) 353–363, http://dx.doi.org/10.1016/S0263-8223(98)00080-4.
[26] Y. Xia, J. Zhu, K. Wang, Q. Zhou, Design and verification of a strain gauge based load sensor for medium-speed dynamic tests with a hydraulic test machine, Int. J. Impact Eng. 88 (2016) 139–152, http://dx.doi.org/10.1016/j.ijimpeng.2015.10.004.
[27] C. Teena Mouni, P. Fayaz Khan, C. Ravishankar, S. Krishnan, S.K. Albert, Addressing the load-ringing phenomena observed at intermediate strain rates to obtain true material response using ensemble empirical mode decomposition, Mater. Lett. 325 (2022) 132778, http://dx.doi.org/10.1016/j.matlet.2022.132778.
[28] H. Wagner, Landing of Seaplanes, NACA Technical Memorandum 622, 1931, pp. 1–23.
[29] S. Seng, Slamming and Whipping Analysis of Ships (Ph.D. thesis), Technical University of Denmark (DTU), Lyngby, Denmark, 2013.
[30] Z. Sun, X.-P. Sui, A. Korobkin, L. Zou, Z. Zong, Slamming force decomposition with gravity effect, J. Fluid. Struct. 114 (2022) 103694, http://dx.doi.org/10.1016/j.jfluidstructs.2022.103694.
[31] A. Tassin, D.J. Piro, A.A. Korobkin, K.J. Maki, M.J. Cooker, Two-dimensional water entry and exit of a body whose shape varies in time, J. Fluid. Struct. 40 (2013) 317–336, http://dx.doi.org/10.1016/j.jfluidstructs.2013.05.002.
[32] R. Hascoët, N. Jacques, Y.-M. Scolan, A. Tassin, A two-dimensional analytical model of vertical water entry for asymmetric bodies with flow separation, Appl. Ocean Res. 92 (2019) http://dx.doi.org/10.1016/j.apor.2019.101878.